International Journal for Numerical and Analytical Methods in Geomechanics
incorporating Mechanics of Cohesive-frictional Materials

Research Article

# A Non-Isothermal Viscoplastic Framework for Assessing Shaft Resistance in Energy Geostructures

**Submission ID** 56395745-cd11-41ca-805d-d78286ad4f0c

**Submission Version** Initial Submission

**PDF Generation** 21 Oct 2025 05:08:44 EST by Atypon ReX

## Authors

Dr. Saeed Tourchi
*Corresponding Author*
*Submitting Author*

ORCiD
https://orcid.org/0000-0001-9720-9940

CRediT
Conceptualization, Investigation, Funding acquisition, Writing - original draft, Methodology, Validation, Visualization, Writing - review & editing, Software, Formal analysis, Project administration, Data curation, Resources

**Affiliations**

- Research Group Computational Soil Mechanics and Foundation Engineering (COMPSOIL), Department of Engineering, Faculty of Science, Technology and Medicine, University of Luxembourg, Luxembourg

Prof. Arash Alimardani Lavasan

CRediT
Validation, Writing - review & editing, Formal analysis, Supervision, Funding acquisition, Investigation, Conceptualization

**Affiliations**

- Research Group Computational Soil Mechanics and Foundation Engineering (COMPSOIL), Department of Engineering, Faculty of Science, Technology and Medicine, University of Luxembourg, Luxembourg

## Files for peer review

All files submitted by the author for peer review are listed below. Files that could not be converted to PDF are indicated; reviewers are able to access them online.

| Name | Type of File | Size | Page |
|---|---|---|---|
| A_Non_Isothermal_Viscoplastic_Framework_for_Assessing_Shaft_Resistance_in_Energy_Geostructures.pdf | Main Document - LaTeX PDF | 1.6 MB | Page 3 |

Received: Added at production | Revised: Added at production | Accepted: Added at production

DOI: xxx/xxxx

RESEARCH ARTICLE

# A Non-Isothermal Viscoplastic Framework for Assessing Shaft Resistance in Energy Geostructures

**Saeed Tourchi** | **Arash Alimardani Lavasan**

[1]Research Group Computational Soil Mechanics and Foundation Engineering (COMPSOIL), Department of Engineering, Faculty of Science, Technology and Medicine, University of Luxembourg, Luxembourg

**Correspondence**
Corresponding author: Saeed Tourchi
Email: saeed.tourchi@uni.lu

## Abstract

This study presents a coupled thermo-hydro-mechanical (THM) numerical investigation of shaft resistance degradation in geothermal piles embedded in low-permeability clays. A thermo-viscoplastic constitutive model is developed to simulate the pile–soil interface behavior under non-isothermal conditions. The model captures the evolution of excess porewater pressure, effective stress reduction, and their combined impact on shaft bearing capacity during thermal activation. Parametric simulations are carried out for a range of fluid temperatures (21–50 °C) and soil permeabilities ($10^{-6}$–$10^{-14}$ $m^2$), representative of in-situ conditions. Results show that undrained heating leads to substantial excess porewater pressure buildup, especially at low permeability and high temperature, resulting in significant reductions in zero-thickness interface element shear strength. A shaft resistance reduction function is proposed to quantify this phenomenon. The numerical predictions are benchmarked against full-scale energy-pile measurements, showing close agreement in temperatures, strains, uplift, and stress. The findings underline the critical role of thermal pressurization in energy pile design and provide an enhanced modeling strategy for performance evaluation in fine-grained soils.

**KEYWORDS**
Geothermal piles, Excess porewater pressure, Shaft resistance, Thermo-hydro-mechanical modeling, Finite element simulation, Energy geostructures

## 1 | INTRODUCTION

The transition toward low-carbon energy systems has brought growing attention to innovative technologies capable of meeting both structural and energy efficiency demands in urban infrastructure. Among these, energy geostructures—particularly energy piles—offer a compelling dual-function solution by combining the mechanical support of deep foundations with the thermal functionality of ground heat exchangers.[1,2,3,4,5,6,7] These systems leverage the stable temperature of the subsurface for heating and cooling applications, thus reducing reliance on fossil fuels and lowering greenhouse gas emissions. Their integration into new and existing buildings supports global objectives for climate resilience and sustainable development, especially in densely populated or retrofitted environments where spatial constraints and energy demands are high.

Thermal activation of structural elements introduces coupled thermo-hydro-mechanical (THM) phenomena that influence both the mechanical behavior and energy performance of the system. In particular, low-permeability soils may exhibit significant thermal pressurization, reducing effective stress and potentially degrading shaft resistance during heating phases[8,9]. These interactions are often neglected in standard design methodologies, despite increasing experimental and numerical evidence of their importance in transient and long-term analyses. As interest in shallow geothermal energy continues to rise, understanding the long-term performance and design challenges of thermally activated geotechnical systems becomes critical for safe, efficient, and resilient deployment.

Thermal loading induces volumetric changes in both the solid skeleton and the pore fluid, generating excess porewater pressure (PWP) when drainage is constrained[10,11,12,13,14,15]. In stiff, low-porosity clays such as Boom Clay, London Clay, and Opalinus Clay, the combination of high plasticity and very low hydraulic conductivity amplifies this effect, often resulting in

  

significant reductions in effective stress under undrained conditions [16,17,18]. This is particularly relevant for geothermal energy piles, where thermal activation causes temperature fluctuations in the vicinity of the pile–soil interface. In such scenarios, the undrained thermal expansion of pore fluid and solid phases leads to excess porewater pressure accumulation, which reduces the effective normal stress and, ultimately, degrades the mobilized shaft resistance [8,19,20]. These effects are further exacerbated during rapid or cyclic thermal loading, typical of seasonal operation of ground source heat pumps, where porewater pressure does not dissipate fully between cycles [21,22,23]. The outcome is a progressive softening of the interface, accompanied by a potential loss of load-bearing capacity over time with repeated cycles.

Beyond mechanical weakening, elevated temperatures can also influence the hydraulic behavior of stiff clays by modifying water viscosity, surface tension, and microstructure, including clay particle arrangement, bonding, and fabric anisotropy [16,24,25,26,20]. Experimental studies have shown that such temperature-induced changes can alter permeability, compressibility, and strength evolution, contributing to highly nonlinear and time-dependent stress path behavior. These findings underscore the critical importance of incorporating coupled THM effects in the design and analysis of energy piles, particularly when embedded in stiff, low-permeability clays where drainage is delayed and thermal gradients are concentrated near the interface.

Despite the growing body of research on energy piles, most existing design approaches and numerical models either neglect the time-dependent behavior of the pile-soil interface or treat thermal effects as simplified boundary conditions. In particular, the long-term evolution of shaft resistance under non-isothermal loading is often approximated using elastic-perfectly plastic or rate-independent models that fail to capture key features such as thermal creep, progressive interface weakening, and loading-rate sensitivity. However, experimental evidence and field observations increasingly indicate that the interface response is not only governed by instantaneous changes in effective stress, but also by the rate and duration of thermal loading, especially under partially or fully undrained conditions [8]. This highlights a critical need to formulate and implement advanced constitutive models that explicitly incorporate the coupled thermo-hydro-mechanical processes occurring at the interface zone.

The present study introduces a non-isothermal viscoplastic constitutive model specifically formulated and implemented for the pile-soil interface, adapted and generalized from a framework originally developed for interface rock joint elements [27]. In this work, the model is reformulated to describe the thermal and rate-dependent behavior of the interface element between energy piles and surrounding low-permeability clays. The constitutive framework captures key features such as temperature-activated yielding, interface creep, and degradation of shaft resistance under sustained or cyclic heating. By implementing this interface model within a fully coupled thermo-hydro-mechanical (THM) finite element formulation [28], the study offers a framework capable of simulating both porewater pressure evolution and stress redistribution at the interface elements of geothermal piles.

To evaluate the influence of governing factors, a comprehensive parametric analysis is performed, exploring the effects of soil permeability, thermal loading intensity, and drainage conditions on excess porewater pressure generation and interface shear stress degradation. A new degradation function is proposed to quantify the progressive reduction in shaft resistance over time. Finally, the model is validated by reproducing the results of the well-documented full-scale energy pile experiment conducted at EPFL [12], which provides insight into the real-world applicability of the framework and highlights the importance of accounting for coupled non-isothermal effects in the design of geothermal foundations.

## 2 | THEORETICAL FORMULATION

### 2.1 | A Non-Isothermal elasto-viscoplastic model for pile–soil interfaces

The behavior of geothermal pile-soil interfaces in stiff, low-permeability clays is governed by highly nonlinear, path-dependent processes involving coupled thermal, mechanical, and time-dependent effects. Experimental observations and field data indicate that thermal loading at these interfaces results in accelerated degradation of shaft resistance and interface stiffness, particularly under cyclic or prolonged thermal cycles. To accurately capture these phenomena, a non-isothermal elasto-viscoplastic constitutive model is developed specifically for zero-thickness interface elements representing the pile–soil contact. The proposed framework incorporates temperature-dependent evolution of interface stiffness and irreversible displacement accumulation, with normal and tangential stiffness parameters defined as functions of temperature and loading rate. The constitutive approach employs a additive decomposition of relative displacement into elastic and viscoplastic components, coupled with thermally modulated softening laws to realistically simulate progressive degradation and time-dependent interface creep. This advanced formulation enables robust prediction of shaft friction loss and interface performance under realistic thermal loading conditions, bridging a critical gap in current geothermal pile design methodologies.

### 2.1.1 | Thermoelastic behavior of pile–soil interface

The localized deformation occurring at the pile–soil interface in geothermal piles is commonly represented using zero-thickness interface elements, where relative displacement arises from discontinuous motion between the pile surface and surrounding soil. In this study, these elements are formulated explicitly to capture the evolution of interface behavior under coupled thermal and mechanical loading conditions. The interface formulation accommodates both elastic and irreversible viscoplastic relative displacements, with interface stiffness and strength properties evolving as functions of temperature and accumulated deformation.

The displacement at the midpoint of the interface element is interpolated from the nodal displacements of adjacent finite elements, taking into account the transformation between the global and local coordinate systems. The temperature-dependent relative displacement vector $\boldsymbol{\delta}_{T,\mathrm{mp}}$ at the interface midpoint is given by:

$$\boldsymbol{\delta}_{T,\mathrm{mp}} = \begin{bmatrix} \delta_{n,T} \\ \delta_{s,T} \end{bmatrix}_{\mathrm{mp}} = r N^{\delta}_{\mathrm{mp}} \begin{bmatrix} -I_4 & I_4 \end{bmatrix} \mathbf{u}_j \tag{1}$$

Here, $\delta_{n,T}$ and $\delta_{s,T}$ represent the normal and tangential components of the temperature-dependent relative displacement, respectively. The rotation matrix $r$ maps local displacements into the global coordinate system, while the shape function matrix $N^{\delta}_{\mathrm{mp}}$ is evaluated at the midpoint of the interface. The vector $\mathbf{u}_j$ contains the nodal displacements corresponding to the nodes defining the interface element. The matrix $\begin{bmatrix} -I_4 & I_4 \end{bmatrix}$ defines the relative displacement between the pile surface (upper nodes) and the surrounding soil (lower nodes). Figure 1 provides a conceptual representation of a zero-thickness interface element embedded along the pile–soil interface, including local definitions of normal and tangential displacements ($\delta_{n,T}$, $\delta_{s,T}$), characteristic interface thickness $h_i$, and element length $dl$.

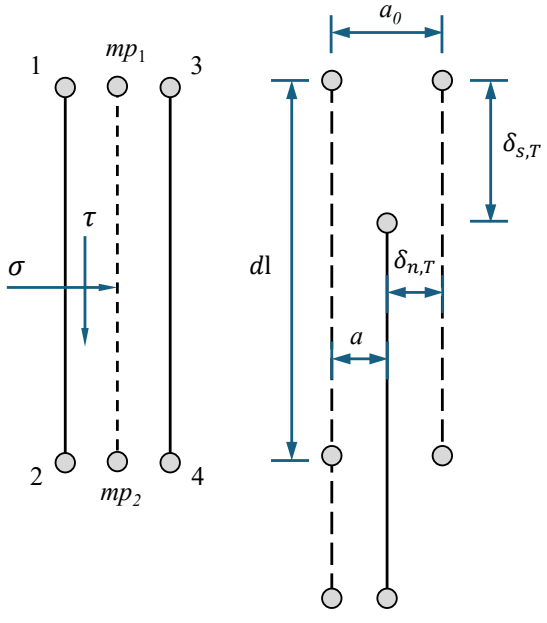


**FIGURE 1** Conceptual representation of a zero-thickness interface element at the pile–soil interface with double nodes.

The stress response at the interface is governed by a linear elastic relationship linking the temperature-dependent relative displacement to the effective normal and tangential interface stresses. This relationship is expressed as:

$$\boldsymbol{\sigma}'_{\mathrm{mp}} = \begin{bmatrix} \sigma' \\ \tau \end{bmatrix}_{\mathrm{mp}} = \mathbf{D}_T \, \boldsymbol{\delta}_{T,\mathrm{mp}} \tag{2}$$

where $\sigma'$ is the effective normal stress acting across the interface, and $\tau$ is the tangential shear stress. The temperature-dependent elastic stiffness matrix $\mathbf{D}_T$ is defined by:

$$\mathbf{D}_T = \begin{bmatrix} K_{n,T} & 0 \\ 0 & K_{s,T} \end{bmatrix} \tag{3}$$

In this formulation, $K_{n,T}$ and $K_{s,T}$ denote the normal and tangential stiffness of the interface, respectively, and these parameters may vary with temperature and deformation history. The effective normal stress is computed by subtracting the porewater pressure acting at the interface from the total normal stress:

$$\sigma'_{\mathrm{mp}} = \sigma_{\mathrm{mp}} - \max(p_{\mathrm{g,mp}}, p_{\mathrm{l,mp}}) \tag{4}$$

Here, $\sigma_{\mathrm{mp}}$ is the total normal stress, while $p_{\mathrm{g,mp}}$ and $p_{\mathrm{l,mp}}$ are the gas and liquid porewater pressures at the interface midpoint, respectively.

The total relative displacement at the geothermal pile–soil interface, $\boldsymbol{\delta}_T$, is decomposed into an elastic component $\boldsymbol{\delta}_T^e$ and a viscoplastic (irreversible) component $\boldsymbol{\delta}_T^{vp}$, reflecting the accumulated slip and deformation along the interface induced by thermal loading cycles. This decomposition can be expressed as:

$$\boldsymbol{\delta}_T = \boldsymbol{\delta}_T^e + \boldsymbol{\delta}_T^{vp} \tag{5}$$

The elastic displacement component, $\boldsymbol{\delta}_T^e$, represents the recoverable deformation directly related to the current effective stress state via the inverse stiffness matrix. In the normal and tangential directions, the elastic interface displacements are defined as follows:

$$\begin{bmatrix} \delta_{n,T}^e \\ \delta_{s,T}^e \end{bmatrix} = \begin{bmatrix} 1/K_{n,T} & 0 \\ 0 & 1/K_{s,T} \end{bmatrix} \begin{bmatrix} \sigma' \\ \tau \end{bmatrix} \tag{6}$$

This relationship implies that higher stiffness values ($K_{n,T}$ and $K_{s,T}$) correspond to smaller elastic relative displacements at a given stress state, whereas temperature-induced stiffness degradation will result in larger interface displacements. Therefore, as thermal loading progressively softens the interface, the elastic displacement components become increasingly significant, emphasizing the importance of explicitly considering thermal influences on stiffness evolution.

To capture the degradation and potential recovery of mechanical properties at the geothermal pile–soil interface under thermal cycles and progressive slip, the stiffness parameters are modeled as functions of both the effective interface thickness and the current temperature. At the reference temperature $T_0$, the normal stiffness is defined through an inverse relationship with the effective thickness of the interface layer:

$$K_{n,T_0} = \frac{m}{a - a_{\min}}, \qquad a = a_0 - \delta_{n,T_0} \tag{7}$$

where $a$ is the instantaneous interface aperture, $a_0$ the initial aperture, $\delta_{n,T_0}$ the normal closure at $T_0$, $a_{\min}$ a small admissible aperture to prevent singularity, and $m$ a calibration parameter. This expression ensures that as the interface narrows due to compaction or densification effects, the interface stiffness correspondingly increases, consistent with experimental observations on clay–structure interfaces.

The stiffness parameter at any given temperature $T$ is further adjusted to account for thermally induced softening or hardening, influenced by the direction and rate of viscoplastic slip accumulation. Accordingly, the temperature-dependent normal stiffness can be expressed as:

$$K_{n,T} = \begin{cases} K_{n,T_0}\left[1 + \mu_{f_K} \ln\left(\dfrac{T}{T_0}\right)\right], & \dot{\delta}_{n,T}^{vp} < \left(\dot{\delta}_{n,T}^{vp}\right)_{\mathrm{tr}} \\ K_{n,T_0}, & \dot{\delta}_{n,T}^{vp} = \left(\dot{\delta}_{n,T}^{vp}\right)_{\mathrm{tr}} \\ K_{n,T_0}\left[1 - \mu_{f_K} \ln\left(\dfrac{T}{T_0}\right)\right], & \dot{\delta}_{n,T}^{vp} > \left(\dot{\delta}_{n,T}^{vp}\right)_{\mathrm{tr}} \end{cases} \tag{8}$$

In this formulation, $\mu_{f_K}$ is a dimensionless parameter characterizing the sensitivity of interface stiffness to temperature changes, and $\left(\dot{\delta}_{n,T}^{vp}\right)_{\mathrm{tr}}$ represents a threshold viscoplastic displacement rate demarcating the transition between thermal hardening and softening behaviors. Under slow displacement rates, thermal effects can strengthen the interface, reflecting increased bonding or consolidation, whereas rapid slip rates result in softening due to thermal weakening of microstructural bonds and fabric deterioration. This adaptive formulation allows realistic simulation of the complex, rate-dependent thermal response observed at geothermal pile–soil interfaces.

The tangential stiffness $K_{s,T}$ governing shear resistance at the pile–soil interface follows a similar temperature- and rate-dependent formulation. It evolves in response to thermal fluctuations and viscoplastic sliding along the tangential direction as:

$$K_{s,T} = \begin{cases} K_{s,T_0}\left[1 + \mu_{f_s} \ln\left(\dfrac{T}{T_0}\right)\right], & \dot{\delta}^{vp}_{s,T} < \left(\dot{\delta}^{vp}_{s,T}\right)_{\text{tr}} \\ K_{s,T_0}, & \dot{\delta}^{vp}_{s,T} = \left(\dot{\delta}^{vp}_{s,T}\right)_{\text{tr}} \\ K_{s,T_0}\left[1 - \mu_{f_s} \ln\left(\dfrac{T}{T_0}\right)\right], & \dot{\delta}^{vp}_{s,T} > \left(\dot{\delta}^{vp}_{s,T}\right)_{\text{tr}} \end{cases} \tag{9}$$

Here, $K_{s,T_0}$ is the reference tangential stiffness at temperature $T_0$, $\mu_{f_s}$ is a dimensionless parameter controlling the sensitivity of tangential stiffness to temperature variations, and $\left(\dot{\delta}^{vp}_{s,T}\right)_{\text{tr}}$ is a threshold viscoplastic slip rate in the tangential direction. Typical values of the threshold rates $\left(\dot{\delta}^{vp}_{n,T}\right)_{\text{tr}}$ and $\left(\dot{\delta}^{vp}_{s,T}\right)_{\text{tr}}$ are determined from interface shear tests and should be treated as calibration parameters for the model. This formulation ensures that the model can capture both thermal hardening (under low-rate slip or mild heating) and thermal softening (under rapid shear and high thermal gradients). Together with the corresponding evolution law in the normal direction, this approach allows the interface element to realistically represent the gradual transition from an initially bonded, stiff interface to a degraded, shear-localized zone with diminished mechanical resistance—an essential feature in simulating the long-term performance of geothermal piles under non-isothermal loading.

### 2.1.2 | Thermal yield surface and strength degradation

In geothermal pile systems, the interface between the pile and surrounding soil experiences complex stress paths due to sustained or cyclic thermal loading. These temperature fluctuations induce not only elastic deformations but also progressive, irreversible slip along the pile–soil interface. To realistically capture the onset and evolution of inelastic response, a thermally regulated yield surface is adopted to govern viscoplastic slip activation. The proposed yield formulation explicitly incorporates temperature-dependent shear strength degradation, accounting for the evolving mechanical behavior of the interface due to both accumulated slip and thermal effects.

The yield function $f_T$ is defined in a smooth, hyperbolic form, offering a continuous transition from elastic to viscoplastic states and enhancing numerical stability relative to sharp-edged criteria such as Mohr-Coulomb:

$$f_T(\sigma', \tau) = \left(\frac{\tau}{q_{u,T}}\right)^2 + \alpha \left(\frac{\sigma'}{q_{u,T}}\right)^2 - 1 \tag{10}$$

Here, $\sigma'$ is the effective normal stress and $\tau$ is the tangential shear stress acting at the pile–soil interface. The parameter $\alpha$ controls the elliptical shape of the yield surface and reflects the coupling between normal and tangential responses. The term $q_{u,T}$ represents the temperature-dependent shear strength envelope of the interface. Yielding occurs when the normalized stress state satisfies $f_T = 0$, indicating initiation of inelastic slip.

The shear strength $q_{u,T}$ evolves dynamically as a function of both normal stress and two temperature-sensitive parameters: cohesion $c_T$ and friction angle $\phi_T$, which are governed by the Mohr-Coulomb strength criterion:

$$q_{u,T} = c_T + \sigma' \tan \phi_T \tag{11}$$

However, unlike classical models, both $c_T$ and $\phi_T$ are treated as internal variables subject to degradation with thermal and mechanical loading. The cohesion $c_T$ is assumed to decrease linearly with respect to accumulated irreversible tangential slip:

$$c_T = c_{0,T}\left(1 - \frac{\delta^{vp}_{s,T}}{\delta_c}\right) \tag{12}$$

where $c_{0,T}$ is the initial cohesion at temperature $T$, $\delta^{vp}_{s,T}$ is the accumulated viscoplastic tangential slip, and $\delta_c$ is a characteristic slip threshold beyond which cohesion fully vanishes. This formulation captures the gradual breakdown of bonding at the interface, as observed in direct shear and pile load tests under elevated temperatures.

Simultaneously, the friction angle $\phi_T$ transitions from a peak value $\phi_{peak,T}$ to a residual value $\phi_{res,T}$ following an exponential decay law:

$$\tan \phi_T = \tan \phi_{res,T} + \left(\tan \phi_{peak,T} - \tan \phi_{res,T}\right) \exp\left(-\beta_d \delta^{vp}_{s,T}\right) \tag{13}$$

The rate of friction angle degradation is controlled by the parameter $\beta_d$, which must be calibrated using interface shear tests under varying thermal and mechanical loading. The residual friction angle $\phi_{res,T}$ is itself a function of temperature, enabling the model to simulate thermal weakening mechanisms associated with suction loss, interparticle bond softening, and lubrication effects in saturated fine-grained soils.

This thermomechanical strength degradation framework allows for realistic modeling of shaft resistance evolution, particularly under long-term heating scenarios where both time- and temperature-dependent softening phenomena are significant. It enables the simulation of progressive interface deterioration, capturing critical processes such as creep, ratcheting, and loss of skin friction capacity in energy piles.

This exponential softening formulation ensures a smooth and continuous evolution of the friction angle as a function of accumulated shear displacement, where the degradation parameter $\beta_d$ controls the rate at which the interface strength deteriorates. Such a formulation is not only physically realistic but also numerically robust, minimizing abrupt strength drops that could otherwise trigger convergence issues in finite element simulations. Importantly, the residual friction angle $\phi_{res,T}$ is defined as a temperature-dependent quantity to reflect well-documented experimental findings: higher temperatures tend to reduce shear strength due to thermally driven loss of interparticle bonding, reduction in suction, and softening of mineral contacts in fine-grained soils.

This temperature dependency is captured using a logarithmic function of the form:

$$\tan \phi_{res,T} = \tan \phi_{res,T_0} \left[ 1 - \xi_\phi \ln \left( \frac{T}{T_0} \right) \right] \tag{14}$$

where $\phi_{res,T_0}$ is the residual friction angle at the reference temperature $T_0$, and $\xi_\phi$ is a material-specific temperature sensitivity coefficient. A positive value of $\xi_\phi$ leads to a progressive decline in residual strength as temperature increases, consistent with observations from heated interface shear tests in saturated stiff clays and low-permeability geomaterials.

The onset and progression of viscoplastic slip are governed by plastic admissibility conditions, defined as:

$$f_T \leq 0, \quad \dot{f}_T = 0 \text{ if } f_T = 0, \quad \dot{\delta}^{vp}_{s,T} \geq 0 \tag{15}$$

These criteria ensure that the interface behaves elastically when the stress state is within the yield surface ($f_T < 0$), and that irreversible slip develops only when the stress state reaches and stays on the yield surface ($f_T = 0$). The irreversibility constraint $\dot{\delta}^{vp}_{s,T} \geq 0$ prohibits reverse plastic flow, in line with the progressive nature of frictional degradation observed in field and laboratory studies on pile–soil interfaces under long-term heating.

### 2.1.3 | Flow rule and viscoplastic slip evolution

Once the yield condition is met, the pile–soil interface undergoes irreversible deformation governed by a viscoplastic flow rule. In this section, we introduce a non-associated, rate-dependent flow formulation that is consistent with experimental observations of clay interfaces, where slip occurs gradually and under thermally influenced conditions. The formulation allows for both shear slip and normal dilation or contraction, depending on the local stress state and temperature.

The direction of viscoplastic flow is defined using a plastic potential function $G_T$, which governs the proportion of slip in the normal and tangential directions. The plastic flow direction is given by:

$$\dot{\boldsymbol{\delta}}^{vp}_T = \dot{\lambda}_T \frac{\partial G_T}{\partial \boldsymbol{\sigma}'} \tag{16}$$

where $\dot{\lambda}_T$ is the temperature-dependent plastic multiplier, and $\partial G_T / \partial \boldsymbol{\sigma}'$ defines the flow direction in stress space. The use of a separate potential function $G_T \neq f_T$ enables a non-associated flow rule, which is necessary to reproduce the dilative or contractive behavior seen in interface shear tests and direct shear experiments.

To avoid numerical singularities and to capture the continuous evolution of deformation near yield, the plastic potential is defined in a smooth, hyperbolic form:

$$G_T(\sigma', \tau) = \sqrt{\tau^2 + \alpha^2 \sigma'^2} - \tau_g \tag{17}$$

Here, $\alpha$ controls the coupling between shear and normal components, and $\tau_g$ is a regularization parameter that governs the shape and position of the flow potential. The square root form ensures differentiability and a smooth transition between sliding

and sticking states. The parameter $\alpha$ may also be calibrated to reflect experimental data, such as dilation angles measured in shear tests at different confining pressures.

The evolution of viscoplastic slip is governed by a rate-dependent law derived from Perzyna-type viscoplasticity, which introduces a time scale into the constitutive response. The rate of plastic displacement is defined by:

$$\dot{\boldsymbol{\delta}}_T^{\mathrm{vp}} = \begin{cases} 0, & f_T < 0, \\ \dot{\lambda}_T \dfrac{\partial G_T}{\partial \boldsymbol{\sigma}'}, & f_T = 0. \end{cases} \tag{18}$$

This condition implies that no viscoplastic deformation occurs while the stress state lies strictly within the yield surface, and plastic flow is activated precisely at the yield threshold.

The rate of the plastic multiplier $\dot{\lambda}_T$ is expressed using a smooth overstress function:

$$\dot{\lambda}_T = \frac{1}{\eta} \left\langle \frac{f_T}{f_0} \right\rangle^n \tag{19}$$

In this relation, $\eta$ is the viscosity coefficient controlling the rate sensitivity of the interface material, $f_0$ is a reference yield function value used to nondimensionalize the overstress, $n$ is the stress exponent that controls the nonlinearity of rate-dependence, and $\langle \cdot \rangle$ is the Macaulay bracket operator defined as $\langle x \rangle = \max(x, 0)$.

The evolution of the accumulated viscoplastic displacement $\delta_{s,T}^{vp}$ is updated at each time step by integrating the viscoplastic slip rate:

$$\delta_{s,T}^{vp}(t + \Delta t) = \delta_{s,T}^{vp}(t) + \dot{\delta}_{s,T}^{vp} \cdot \Delta t \tag{20}$$

This cumulative displacement is used as an internal variable in the strength degradation functions for cohesion and friction angle, closing the loop between mechanical behavior, temperature effects, and material degradation. The proposed viscoplastic flow rule thus allows the model to capture realistic time-dependent interface behavior, including creep-like sliding under sustained load, rate effects during rapid shearing, and stiffness degradation due to temperature rise and accumulated slip.

## 2.2 | Mass fluxes in the local interface frame

We use a local orthonormal frame attached to the pile–soil interface: $n$ is the unit normal (pointing from the interface into the soil) and $s$ is the unit tangential direction along the interface.

The liquid-phase (advective) mass flux follows Darcy's law

$$\mathbf{q}_l = -\frac{\mathbf{k}_l}{\mu_l} \left( \nabla p_l - \rho_l \mathbf{g} \right), \tag{21}$$

where $\mathbf{k}_l$ is the intrinsic permeability tensor of the interface zone/adjacent soil, $\mu_l$ is the dynamic viscosity of water, $p_l$ is liquid pressure, $\rho_l$ is liquid density, and $\mathbf{g}$ is gravity. In the local $(n, s)$ frame:

$$q_l^{\perp} = -\frac{k_l^{\perp}}{\mu_l} \left( \frac{\partial p_l}{\partial n} - \rho_l g_n \right), \tag{22}$$

$$q_l^{\parallel} = -\frac{k_l^{\parallel} \, k_{l,\parallel}^{\mathrm{rel}}(S_l)}{\mu_l} \left( \frac{\partial p_l}{\partial s} - \rho_l g_s \right), \tag{23}$$

where $k_l^{\perp}$ and $k_l^{\parallel}$ are the normal and tangential components of intrinsic permeability, $k_{l,\parallel}^{\mathrm{rel}}(S_l)$ is the relative permeability (e.g., van Genuchten–Mualem) as a function of liquid saturation $S_l$, and $g_n = \mathbf{g} \cdot \mathbf{n}$, $g_s = \mathbf{g} \cdot \mathbf{s}$. (If partial saturation significantly affects normal drainage, $k_{l,\parallel}^{\mathrm{rel}}$ can also be applied to $q_l^{\perp}$.)

Vapor-phase diffusion is modeled with Fick's law along the interface:

$$i_g^{w,\parallel} = -D_g^{w,\parallel} \frac{\partial Y_g^w}{\partial s} \tag{24}$$

where $i_g^{w,\parallel}$ is the diffusive mass flux of water in the gas phase per unit area (tangential), $D_g^{w,\parallel}$ is the effective binary diffusion coefficient of water vapor in air along the interface, and $Y_g^w$ is the mass fraction of water in the gas phase. No gravity term appears in diffusion.

All pressures are denoted by lower-case $p$ and are in Pa; intrinsic permeabilities $k$ are in $m^2$; $\mu_l$ in Pa s; densities in kg $m^{-3}$; diffusion coefficients $D$ in $m^2$ $s^{-1}$. The superscripts $\perp$ and $\parallel$ refer to normal and tangential components. Relative permeabilities $k_l^{\mathrm{rel}}(\cdot)$ are dimensionless. We report permeability as the intrinsic permeability $k$ ($m^2$) unless stated otherwise. Hydraulic conductivity $K$ (m $s^{-1}$) is related to the intrinsic permeability $k$ by $K = (\rho_l g/\mu_l)\, k$; equivalently $k = (\mu_l/(\rho_l g))\, K$. Unless specified, water properties are taken at 20 °C.

The hydraulic conductivity along the pile–soil interface direction is estimated using the cubic law:

$$K_I = \frac{\rho g}{\mu_f} \frac{e^3}{12} \tag{25}$$

where $\rho$ denotes fluid density, $g$ the gravitational acceleration, and $\mu_f$ the viscosity of the fluid. The intrinsic permeability can therefore be expressed as follows:

$$k_{ll} = \frac{e^2}{12} \tag{26}$$

The hydraulic aperture ($e$) at the pile–soil interface can be connected to its geometric aperture ($a$) and roughness parameter ($r_i$), based on the relationship introduced by [29]. By employing Barton's formulation, the expression for the intrinsic permeability along the longitudinal direction becomes:

$$k_{ll} = \frac{1}{12} \left( \frac{a}{(r_i)^{2.5}} \right)^2 \tag{27}$$

The transverse intrinsic permeability $k_{lt}$ is assumed to be equal to that of the surrounding porous medium. The saturation level of the interface is determined using the standard retention curve suggested by [30]:

$$S_l = \left[ 1 + \left( \frac{s}{P} \right)^{\frac{1}{1-\lambda}} \right]^{-\lambda} \tag{28}$$

The current suction is defined as $s = p_g - p_l$, where $p_g$ and $p_l$ represent the gas and liquid pressures, respectively. Here, $\lambda$ is the van Genuchten shape parameter (often denoted by $\lambda^*$ in other formulations), and $P$ denotes the air entry pressure required to initiate desaturation at the interface.

The air entry pressure of the pile–soil interface is influenced by the hydraulic aperture. This relationship can be interpreted through the Laplace equation, where the air entry pressure depends on the surface tension, contact angle, and the characteristic size of the aperture, and can be further linked to the ratio between the current and reference intrinsic permeabilities:

$$P = P_0 \sqrt{\frac{k_{l0}}{k_l}} \tag{29}$$

Moreover, when temperature-dependent phenomena are accounted for, the value of $P$ is adjusted by the surface tension, $\sigma$:

$$P = P_0 \sqrt{\frac{k_{l0}}{k_l}} \frac{\sigma}{\sigma_0} \tag{30}$$

The relative permeability is calculated by

$$k_{\mathrm{rel}}^l = A S_l^n \tag{31}$$

where the exponent and prefactor are set to n=3 and A=1 for all cases considered here—commonly used values representing a simplified form of the van Genuchten–Mualem model.

Fourier's law gives the heat conduction:

$$i_C = -\lambda \nabla T \tag{32}$$

where $\lambda$ denotes the effective thermal conductivity of the interface element, and $\nabla T$ is the temperature gradient. To account for the influence of moisture content, $\lambda$ is modeled as a function of the liquid saturation degree $S_l$, using a widely adopted empirical mixing law:

$$\lambda = \lambda_{\text{sat}}\sqrt{S_l} + \lambda_{\text{dry}}(1 - \sqrt{S_l}) \tag{33}$$

Here, $\lambda_{\text{sat}}$ and $\lambda_{\text{dry}}$ represent the thermal conductivities under saturated and dry conditions, respectively. The square root form captures the nonlinear increase of thermal conductivity with saturation and reflects experimental observations in soils and clay-rich geomaterials.

## 2.3 | THM formulation: balance equations (after Alonso et al.[31])

The behavior of two-phase flow within the pile–soil interface elements is characterized by deriving the governing equations for mass and energy conservation of water and air at the interface. Water may exist in both the liquid and vapor phases. The overall mass balance of water for a differential segment of the interface element is given as:

$$\frac{\partial(\theta_{\text{l}}^{\text{w}} S_{\text{l}} + \theta_{\text{g}}^{\text{w}} S_{\text{g}})}{\partial t} a \, \mathrm{d}l + (\theta_{\text{l}}^{\text{w}} S_{\text{l}} + \theta_{\text{g}}^{\text{w}} S_{\text{g}}) \frac{\mathrm{d}a}{\mathrm{d}t} \, \mathrm{d}l + [\boldsymbol{J}_{\text{l}}^{\text{w}}]_{\text{mp}} + [\boldsymbol{J}_{\text{g}}^{\text{w}}]_{\text{mp}} = f^{\text{w}} \tag{34}$$

where $\theta_{\text{l}}^{\text{w}}$ and $\theta_{\text{g}}^{\text{w}}$ represent the water content in the liquid and vapor phases, respectively. The parameter $a$ indicates the hydraulic aperture of the pile–soil interface element, and $\mathrm{d}l$ is its representative length. The saturation degrees in the liquid and gas phases are denoted by $S_{\text{l}}$ and $S_{\text{g}}$, respectively. The terms $[\boldsymbol{J}_{\text{l}}^{\text{w}}]_{\text{mp}}$ and $[\boldsymbol{J}_{\text{g}}^{\text{w}}]_{\text{mp}}$ correspond to the fluxes of liquid and vapor water through the interface, while $f^{\text{w}}$ denotes an external source term contributing to water mass.

$$\begin{aligned} [\boldsymbol{J}_{\text{l}}^{\text{w}}]_{\text{mp}} &= [\theta_{\text{l}}^{\text{w}} \boldsymbol{q}_{\text{lt}} \, \mathrm{d}l + \boldsymbol{i}_{\text{lt}}^{\text{w}} \, \mathrm{d}l]_0^a + [\theta_{\text{l}}^{\text{w}} \boldsymbol{q}_{\text{ll}} \, a + \boldsymbol{i}_{\text{ll}}^{\text{w}} \, a]_0^{\mathrm{d}l} \\ [\boldsymbol{J}_{\text{g}}^{\text{w}}]_{\text{mp}} &= [\theta_{\text{g}}^{\text{w}} \boldsymbol{q}_{\text{gt}} \, \mathrm{d}l + \boldsymbol{i}_{\text{gt}}^{\text{w}} \, \mathrm{d}l]_0^a + [\theta_{\text{g}}^{\text{w}} \boldsymbol{q}_{\text{gl}} \, a + \boldsymbol{i}_{\text{gl}}^{\text{w}} \, a]_0^{\mathrm{d}l} \end{aligned} \tag{35}$$

where $\boldsymbol{q}_{\text{lt}}$, $\boldsymbol{q}_{\text{gt}}$, $\boldsymbol{q}_{\text{ll}}$, and $\boldsymbol{q}_{\text{gl}}$ denote the advective flux vectors (for liquid and gas phases) in the transverse and longitudinal directions at the boundaries of the interface element. Similarly, $\boldsymbol{i}_{\text{lt}}^{\text{w}}$, $\boldsymbol{i}_{\text{gt}}^{\text{w}}$, $\boldsymbol{i}_{\text{ll}}^{\text{w}}$, and $\boldsymbol{i}_{\text{gl}}^{\text{w}}$ represent the corresponding non-advective flux vectors.

The air mass balance formulation accounts for both free air and air dissolved in the liquid phase. Its mathematical form is provided below:

$$\frac{\partial(\theta_{\text{l}}^{\text{a}} S_{\text{l}} + \theta_{\text{g}}^{\text{a}} S_{\text{g}})}{\partial t} a \, \mathrm{d}l + (\theta_{\text{l}}^{\text{a}} S_{\text{l}} + \theta_{\text{g}}^{\text{a}} S_{\text{g}}) \frac{\mathrm{d}a}{\mathrm{d}t} \, \mathrm{d}l + [\boldsymbol{J}_{\text{l}}^{\text{a}}]_{\text{mp}} + [\boldsymbol{J}_{\text{g}}^{\text{a}}]_{\text{mp}} = f^{\text{a}} \tag{36}$$

where $\theta_{\text{l}}^{\text{a}}$ represents the air content dissolved in the liquid phase, and $\theta_{\text{g}}^{\text{a}}$ refers to the amount of air in the gas (dry) phase. The term $[\boldsymbol{J}_{\text{l}}^{\text{a}}]_{\text{mp}}$ corresponds to the dissolved air flux vector at the pile–soil interface, while $[\boldsymbol{J}_{\text{g}}^{\text{a}}]_{\text{mp}}$ denotes the gas-phase air flux vector. The parameter $f^{\text{a}}$ accounts for any external input of air to the system.

The thermal energy content associated with the liquid and gas phases is determined using the following expressions:

$$\frac{\partial(E_{\text{l}}\rho_{\text{l}} S_{\text{l}} + E_{\text{g}}\rho_{\text{g}} S_{\text{g}})}{\partial t} a \, \mathrm{d}l + (E_{\text{l}}\rho_{\text{l}} S_{\text{l}} + E_{\text{g}}\rho_{\text{g}} S_{\text{g}}) \frac{\mathrm{d}a}{\mathrm{d}t} \, \mathrm{d}l + [\boldsymbol{i}_{\text{c}}]_{\text{mp}} + [\boldsymbol{J}_{\text{El}}]_{\text{mp}} + [\boldsymbol{J}_{\text{Eg}}]_{\text{mp}} = f^E \tag{37}$$

The energies linked to the liquid and gas phases are determined by:

$$\begin{aligned} E_{\text{l}}\rho_{\text{l}} &= (E_{\text{l}}^{\text{w}}\omega_{\text{l}}^{\text{w}} + E_{\text{l}}^{\text{a}}\omega_{\text{l}}^{\text{a}})\rho_{\text{l}} = E_{\text{l}}^{\text{w}}\theta_{\text{l}}^{\text{w}} + E_{\text{l}}^{\text{a}}\theta_{\text{l}}^{\text{a}} \\ E_{\text{g}}\rho_{\text{g}} &= (E_{\text{g}}^{\text{w}}\omega_{\text{g}}^{\text{w}} + E_{\text{g}}^{\text{a}}\omega_{\text{g}}^{\text{a}})\rho_{\text{g}} = E_{\text{g}}^{\text{w}}\theta_{\text{g}}^{\text{w}} + E_{\text{g}}^{\text{a}}\theta_{\text{g}}^{\text{a}} \end{aligned} \tag{38}$$

where $E_{\text{l}}^{\text{w}}$ and $E_{\text{l}}^{\text{a}}$ refer to the specific internal energies (per unit mass) of water and air within the liquid phase. The symbols $\omega_{\text{l}}^{\text{w}}$ and $\omega_{\text{l}}^{\text{a}}$ indicate the corresponding masses of water and air in the liquid phase. Similarly, $E_{\text{g}}^{\text{w}}$ and $E_{\text{g}}^{\text{a}}$ denote the specific internal energies of water and air in the gas phase, while $\omega_{\text{g}}^{\text{w}}$ and $\omega_{\text{g}}^{\text{a}}$ represent their respective masses. The densities of the liquid and gas phases are denoted by $\rho_{\text{l}}$ and $\rho_{\text{g}}$, respectively.

The specific internal energies of the liquid and gas phases are denoted by $E_{\text{l}}$ and $E_{\text{g}}$. The term $[\boldsymbol{i}_{\text{c}}]_{\text{mp}}$ corresponds to the conductive heat flux vector through the zero-thickness interface. The quantities $[\boldsymbol{J}_{\text{El}}]_{\text{mp}}$ and $[\boldsymbol{J}_{\text{Eg}}]_{\text{mp}}$ represent the advective energy flux vectors associated with the liquid and gas phases at the interface.

$$[\boldsymbol{i}_{\text{c}}]_{\text{mp}} = [\boldsymbol{i}_{\text{ct}} \, \mathrm{d}l]_0^a + [\boldsymbol{i}_{\text{cl}} \, a]_0^{\mathrm{d}l} \tag{39}$$

where $\boldsymbol{i}_{\text{ct}}$ and $\boldsymbol{i}_{\text{cl}}$ represent the heat flux vectors in the transverse and longitudinal directions at the boundaries of the interface element, respectively.

The quantities $[\boldsymbol{J}_{\text{El}}]_{\text{mp}}$ and $[\boldsymbol{J}_{\text{Eg}}]_{\text{mp}}$ are determined by evaluating the advective transport of energy, as follows:

$$[\boldsymbol{J}_{\mathrm{El}}]_{\mathrm{mp}} = [\boldsymbol{J}_{\mathrm{l}}^{\mathrm{w}}]_{\mathrm{mp}} E_{\mathrm{l}}^{\mathrm{w}} + [\boldsymbol{J}_{\mathrm{l}}^{\mathrm{a}}]_{\mathrm{mp}} E_{\mathrm{l}}^{\mathrm{a}}$$
$$[\boldsymbol{J}_{\mathrm{Eg}}]_{\mathrm{mp}} = [\boldsymbol{J}_{\mathrm{g}}^{\mathrm{w}}]_{\mathrm{mp}} E_{\mathrm{g}}^{\mathrm{w}} + [\boldsymbol{J}_{\mathrm{g}}^{\mathrm{a}}]_{\mathrm{mp}} E_{\mathrm{g}}^{\mathrm{a}} \tag{40}$$

The balance equations are solved in a coupled manner. The primary unknowns at each node consist of the normal and tangential relative displacements ($\delta_{n,T}$, $\delta_{\mathrm{s}}$), gas and liquid pressures ($p_{\mathrm{g}}$, $p_{\mathrm{l}}$), and temperature $T$.

Advective flow along the longitudinal direction is governed by Darcy's law. Diffusive transport, or non-advective fluxes, is represented using Fick's law. The hydraulic properties of the pile–soil interface, including permeability and air entry pressure, are influenced by the aperture size. Heat conduction across the interface is evaluated according to Fourier's law.

## 3 | NUMERICAL SIMULATION OF THE EPFL IN-SITU ENERGY PILE TEST

To validate the proposed thermo-hydro-mechanical (THM) framework for simulating pile–soil interface behavior under thermal loading, a comprehensive numerical model was developed to replicate the well-documented in-situ energy pile test conducted at the Swiss Federal Institute of Technology in Lausanne (EPFL)[12]. This experimental campaign provides an extensive dataset capturing the coupled thermo-mechanical response of a full-scale heat exchanger pile under combined mechanical and thermal loading conditions, making it an ideal benchmark for validating advanced numerical models.

### 3.1 | Experimental configuration and site characterization

The EPFL test pile was constructed as part of a four-storey building foundation system, comprising 97 piles approximately 25 m in length. The instrumented test pile, located at the building perimeter to minimize group effects, featured a drilled shaft with a diameter of 0.88 m and a total length of 25.8 m. The pile was equipped with polyethylene (PE) tubes arranged in a U-shaped configuration to facilitate the circulation of heat-carrying fluid, representing a typical geothermal energy pile configuration.

The site stratigraphy consists of five distinct geological layers, as characterized through investigations and static pile load tests[12]. The soil $A_1$ (0–5 m): alluvial deposits with moderate permeability; (ii) Layer $A_2$ (5–10 m): secondary alluvial formations; (iii) Layer B (10–22 m): sandy gravelly moraine with enhanced drainage characteristics; (iv) Layer C (22–26 m): bottom moraine with reduced permeability; and (v) Layer D (26+ m): molasse bedrock formation with very low permeability. The groundwater table is located near the ground surface, creating fully saturated conditions throughout the pile length.

Extensive instrumentation was deployed to monitor the pile's thermo-mechanical response, including 28 vibrating-wire extensometers for vertical strain and temperature measurements, 24 fiber-optic extensometers (1 m length) for vertical strain monitoring, 5 fiber-optic extensometers (2 m length) for radial strain measurements at five depths, one load cell at the pile base, and four extensometers at the pile head for vertical displacement monitoring. This comprehensive instrumentation array enabled detailed validation of numerical predictions across multiple response parameters.

### 3.2 | Numerical model development

The computational domain was defined as a 50 m × 50 m two-dimensional axisymmetric section, taking advantage of the circular pile geometry and horizontally stratified soil profile. The energy pile was positioned at the domain center, surrounded by the layered soil profile extending to sufficient depth to minimize boundary effects. To ensure numerical accuracy and capture steep gradients around the pile–soil interface, the domain was discretized using 533 quadrilateral elements and 582 nodes, with mesh refinement concentrated in the vicinity of the pile to accurately resolve interface behavior and thermal/hydraulic gradients (Figure 2).

The soil layers were characterized using material properties derived from comprehensive laboratory testing programs, including triaxial tests on samples from layers A, B, and C, as well as in-situ permeability measurements[12]. Each layer was assigned specific mechanical, hydraulic, and thermal properties, including Young's modulus, Poisson's ratio, permeability, thermal conductivity, specific heat capacity, and thermal expansion coefficients. The material parameters are summarized in Table 1, reflecting the heterogeneous nature of the site stratigraphy.

The reinforced concrete energy pile was modeled using linear elastic behavior with a Young's modulus of 29.2 GPa, determined through laboratory tests and cross-hole ultrasonic transmission measurements. The elastic modulus accounts for the composite

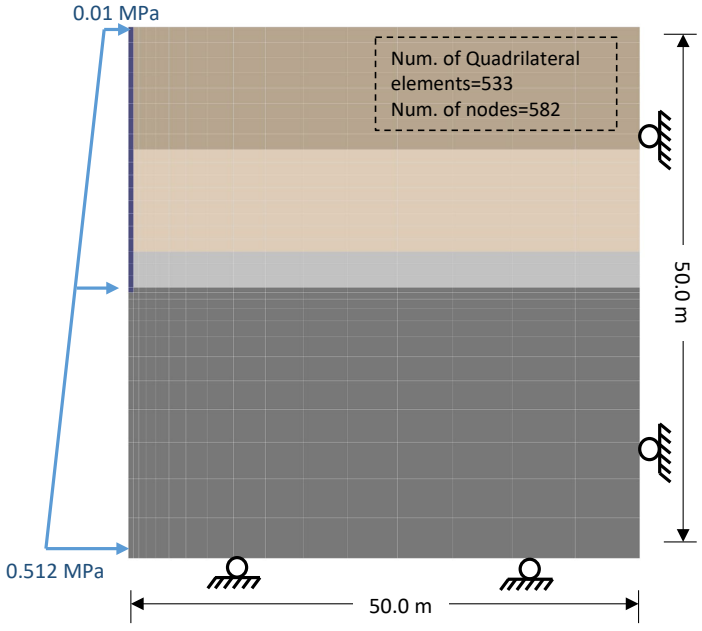


**FIGURE 2** Model geometry, boundary conditions and finite element mesh employed.

**TABLE 1** Material properties of soil layers, reinforced concrete elements, and HDPE pipes derived from EPFL site characterization [12].

| Material | $E$ (MPa) | $\nu$ | $n$ | $\rho_s$ (kg/m$^3$) | $c_{p,s}$ (J/kg·°C) | $\lambda_s$ (W/m·°C) | $\alpha$ (1/°C) |
|---|---|---|---|---|---|---|---|
| **Soil layers** | | | | | | | |
| $A_1$ (Alluvial) | 190 | 0.22 | 0.10 | 2769 | 880 | 1.49 | $3.3 \times 10^{-6}$ |
| $A_2$ (Alluvial) | 190 | 0.22 | 0.10 | 2769 | 880 | 1.49 | $3.3 \times 10^{-6}$ |
| B (Sandy moraine) | 84 | 0.40 | 0.35 | 2735 | 890 | 3.68 | $3.3 \times 10^{-6}$ |
| C (Bottom moraine) | 90 | 0.40 | 0.30 | 2740 | 890 | 3.46 | $3.3 \times 10^{-6}$ |
| D (Molasse) | 3000 | 0.30 | 0.10 | 2167 | 923 | 3.82 | $2.3 \times 10^{-5}$ |
| **Reinforced concrete elements** | | | | | | | |
| Energy pile | 29200 | 0.25 | 0.10 | 2500 | 837 | 1.628 | $1.0 \times 10^{-5}$ |
| Structural slab | 35000 | 0.25 | 0.10 | 2722 | 837 | 1.628 | $1.0 \times 10^{-5}$ |
| **Heat exchanger system** | | | | | | | |
| HDPE pipes | — | — | — | — | — | 0.42 | — |

nature of reinforced concrete, incorporating both concrete matrix and steel reinforcement contributions. The structural slab was assigned a higher stiffness (35 GPa) to represent the increased reinforcement density typical of building slabs.

## 3.3 | Interface modeling and constitutive framework

The pile–soil interface was simulated using the non-isothermal elasto-viscoplastic interface model developed in section 2.1. The interface formulation incorporates temperature-dependent stiffness degradation, thermally-activated strength reduction, and rate-dependent viscoplastic flow to capture the complex behavior observed during thermal loading cycles. The constitutive model parameters were calibrated through in-situ measurements, with particular attention to capturing the observed thermal strain evolution and pile displacement patterns.

**TABLE 2** Constitutive model parameters for the pile–soil interface, calibrated against EPFL experimental data.

| Parameter | Symbol | Value |
|---|---|---|
| Initial cohesion at reference temperature | $c_{0,T_0}$ (MPa) | 0.25 |
| Peak friction angle | $\phi_{peak,T_0}$ (°) | 24 |
| Residual friction angle | $\phi_{res,T_0}$ (°) | 16 |
| Cohesion degradation threshold | $\delta_c$ (mm) | 5.0 |
| Friction angle degradation rate | $\beta_d$ (mm$^{-1}$) | 0.8 |
| Normal stiffness at $T_0$ | $K_{n,T_0}$ (MPa/m) | $2.0 \times 10^5$ |
| Tangential stiffness at $T_0$ | $K_{s,T_0}$ (MPa/m) | $1.0 \times 10^5$ |
| Stiffness degradation rate | $\mu_{f_K}, \mu_{f_s}$ | 0.15 |
| Yield surface shape parameter | $\alpha$ | 0.35 |
| Viscosity coefficient | $\eta$ (MPa·s) | $1.0 \times 10^6$ |
| Stress exponent | $n$ | 5 |
| Plastic potential threshold | $\tau_g$ (MPa) | 0.10 |
| Temperature sensitivity coefficient | $\xi_\phi$ | 0.10 |
| Reference yield function value | $f_0$ | 1.0 |

## 3.4 | Boundary conditions and loading protocol

The mechanical boundary conditions were prescribed to replicate the experimental configuration, with vertical displacements fixed at the domain base and roller supports constraining horizontal movement at the lateral boundaries. A constant vertical stress of 0.21 MPa was applied to the top boundary to simulate the construction load from the overlying building structure. The initial temperature throughout the domain was uniformly set to 13.4°C, corresponding to the natural ground temperature measured at the site.

Hydraulic boundary conditions were implemented to represent the site's hydrogeological conditions, with hydrostatic porewater pressure distribution ranging from 0.01 MPa at the surface to 0.512 MPa at the base, reflecting the natural groundwater gradient. Drainage was permitted at the ground surface and lateral boundaries for permeable layers, while the molasse formation (Layer D) was treated as impermeable, consistent with field observations.

The thermal loading protocol was designed to replicate Test 1 of the EPFL experimental campaign, which involved a heating–cooling cycle with the pile head free to move vertically. During the heating phase, a temperature increment of 21°C was applied at the pile–soil interface over a period of 12 days, followed by a cooling phase extending over 16 days during which the interface temperature gradually returned to ambient conditions. This loading sequence represents a typical operational cycle for geothermal energy piles and provides comprehensive data for model validation.

# 4 | MODEL VALIDATION

The simulation was conducted using fully coupled thermo-hydro-mechanical (THM) analysis to capture the complex interactions between thermal expansion, porewater pressure evolution, and mechanical stress redistribution. Time-dependent calculations employed small time increments (typically 0.25 days) to accurately resolve transient phenomena, particularly those related to temperature propagation and porewater pressure generation/dissipation in low-permeability zones.

The thermal loading was applied through Dirichlet boundary conditions at the pile interface, ensuring controlled and consistent thermal input that matches the experimental temperature evolution. The heat exchanger system within the pile was not explicitly modeled; instead, its thermal influence was incorporated through prescribed temperature boundary conditions derived from experimental measurements, providing a computationally efficient approach while maintaining physical realism.

To evaluate the accuracy of the proposed thermo-hydro-mechanical (THM) framework, simulation results were compared against experimental measurements from Test 1 of the EPFL in-situ energy pile campaign. This test involved a heating–cooling cycle consisting of 12 days of thermal loading followed by 16 days of passive cooling. Both temperature and stress responses were monitored at multiple depths along the pile using optical fiber sensors, extensometers, and load cells. The numerical model was configured to replicate this loading sequence and boundary setup, as described in previous sections.

## 4.1 | Thermal response

The simulation successfully reproduced the observed thermal evolution during the heating-cooling cycle. As shown in Figure 3a, the imposed interface temperature rose progressively during the heating phase and dropped in a nonlinear fashion during the cooling stage, matching the shape and amplitude of the experimental temperature curve. The peak temperature increment of approximately 21°C occurred around day 12 and decreased steadily thereafter, consistent with field observations. As shown in Figure 4, the day-12 contours concentrate along the pile—indicating strong local heating and steep gradients—whereas at day 28 the contours are more diffuse and move into the far field, reflecting reduced peak temperatures and ongoing thermal equilibration.

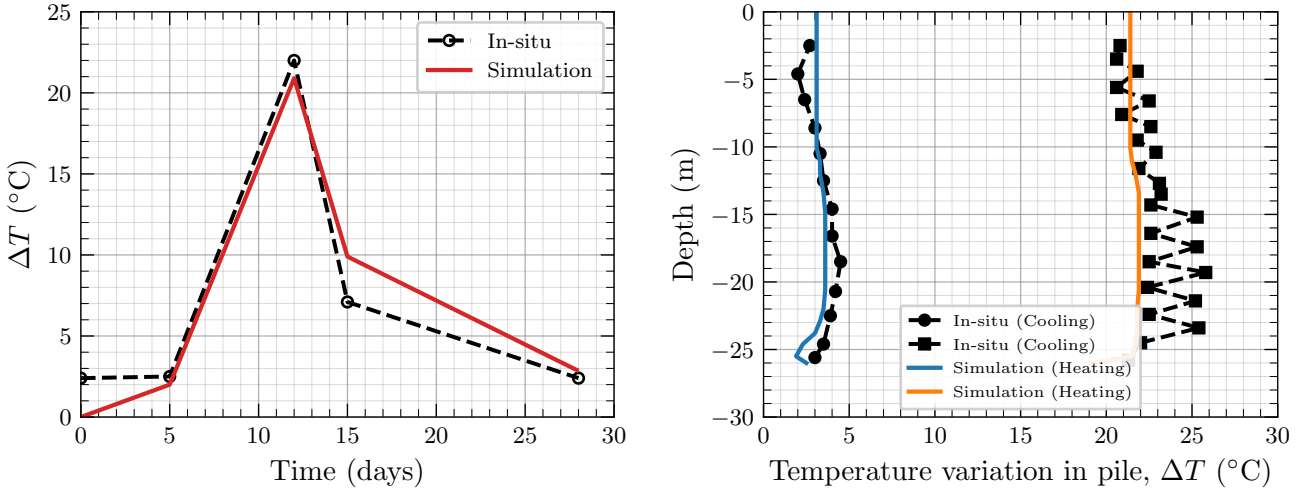


**FIGURE 3** (a) Interface temperature evolution during the heating–cooling cycle; (b) Temperature increment profiles along the pile depth. Experimental measurements vs numerical simulation.

The spatial distribution of temperature along the pile was also captured accurately. Figure 3b compares the numerically imposed and experimentally measured temperature increments at different depths. The simulation reproduced the stratification in thermal response, which is influenced by the varying thermal properties of the soil layers and the boundary dissipation conditions. Minor discrepancies near the pile head are attributed to the smoothing of the applied boundary condition in the numerical model.

## 4.2 | Thermomechanical response

### 4.2.1 | Axial and Radial Thermal Strain

The imposed temperature gradient caused axial expansion of the pile, which in turn generated measurable vertical strains along the shaft. Figure 5a presents the comparison between simulated and measured axial strain profiles during both heating and cooling phases. The model accurately reproduced the magnitude and distribution of vertical strain. Strains were highest near the mid-depth of the pile, where friction mobilization is most active. During cooling, the thermal contraction led to strain reversal, although full symmetry was not achieved due to residual stress buildup and partial recovery of temperature.

In addition to axial response, radial strain behavior was simulated to assess the pile–soil contact interaction. Figure 5b shows the time evolution of radial strain at a depth of 16 m. The model exhibited good agreement with the measured response, capturing both the increase in radial expansion during heating and the reduction during cooling. Importantly, the simulation confirmed that lateral contact between the pile and soil was preserved throughout the cycle, as evidenced by the non-zero residual strain at the end of cooling.

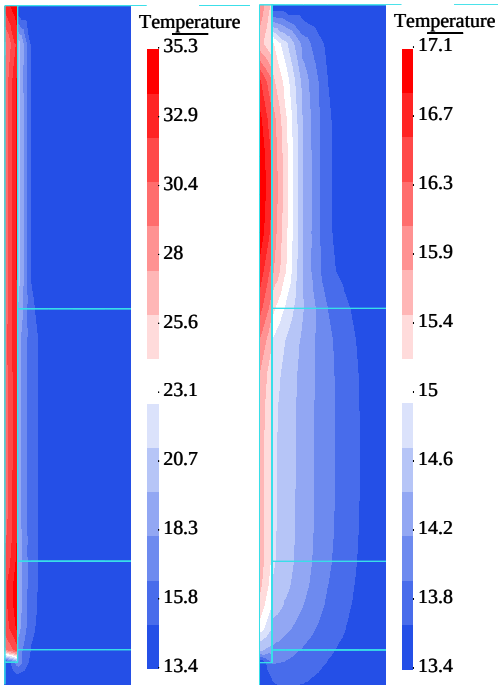


**FIGURE 4** Computed contours of equal temperature (°C) for (a) heating (day 12); (b) cooling (day 28).

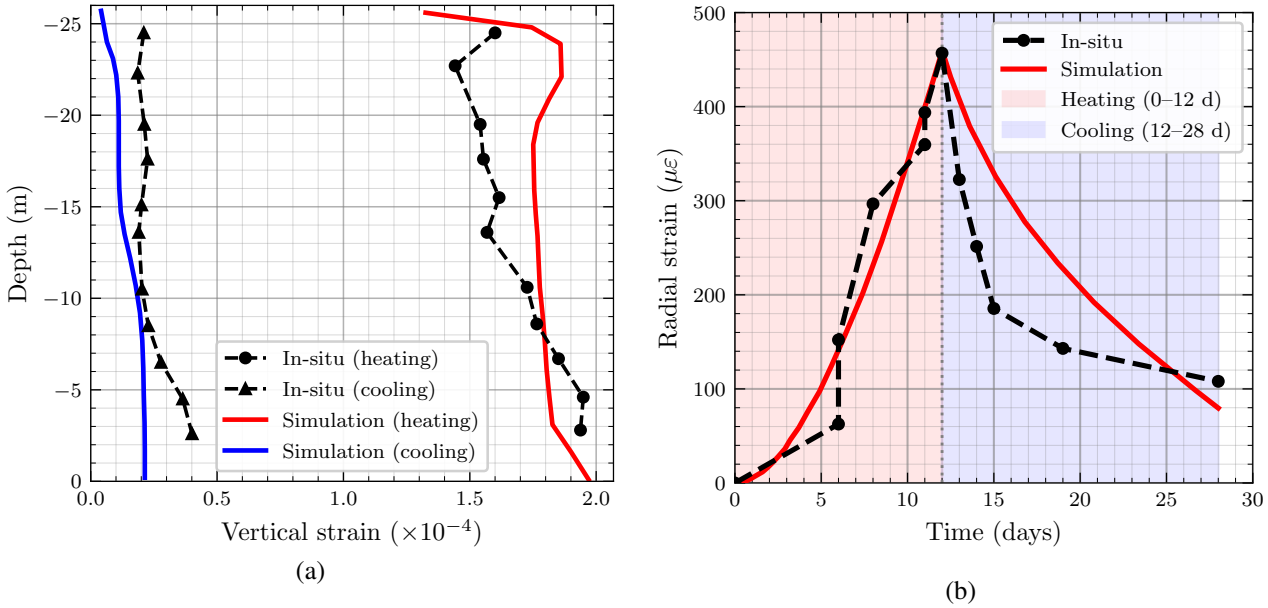


**FIGURE 5** (a) Vertical strain profiles measured and simulated under cooling and heating conditions; (b) Time evolution of radial strain at the pile–soil interface under thermal loading.

### 4.2.2 | Vertical displacement (Pile Uplift)

One of the key quantities of interest in geothermal pile systems is the pile head displacement due to thermal activation. Figure 6 compares the vertical uplift predicted by the model against optical fiber measurements. A peak displacement of approximately 3.5 mm was observed at the end of the heating period, followed by partial reversal during cooling. The model reproduced this

behavior well, with good agreement in both magnitude and timing. A contour map of vertical displacement at peak uplift further illustrates the influence of thermal expansion and interface friction (Figure 7).

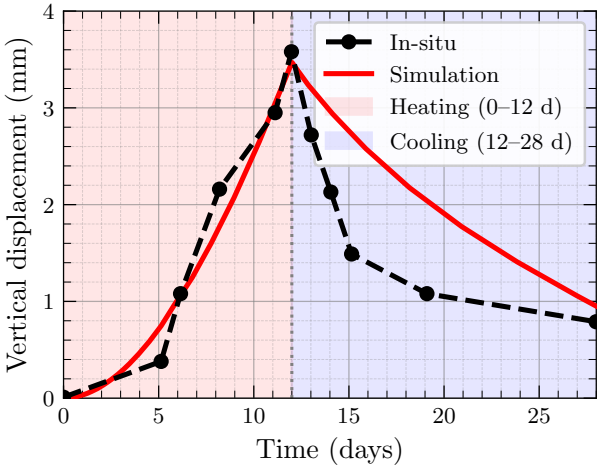


**FIGURE 6** Evolution of vertical head displacement over time under thermal loading.

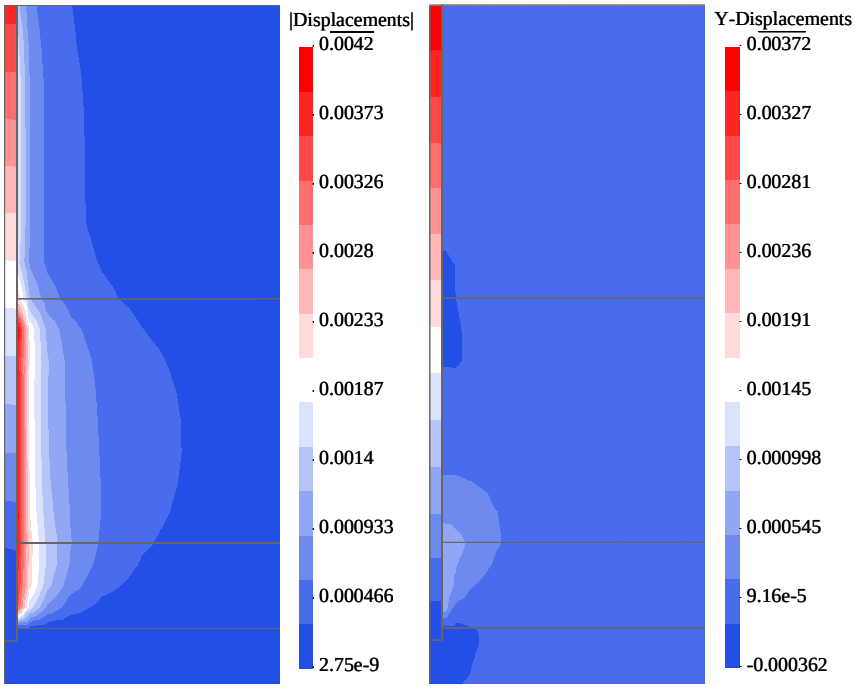


**FIGURE 7** Computed contours of (left) total displacements (mm); (right) vertical displacements at the end of heating.

### 4.2.3 | Induced thermal stresses

The thermal strain imposed on the pile also induced vertical stresses along the shaft due to constraint from the surrounding soil. Figure 8 compares the simulated and measured vertical stress distribution at day 15, corresponding to the peak heating phase. The simulation captures the layer-dependent stress profile and the influence of soil stratigraphy (layers A through D). High stress concentration zones were observed near the transitions between layers, consistent with measured data. This validates the model's ability to account for variable soil stiffness and interface frictional behavior under thermally induced loading.

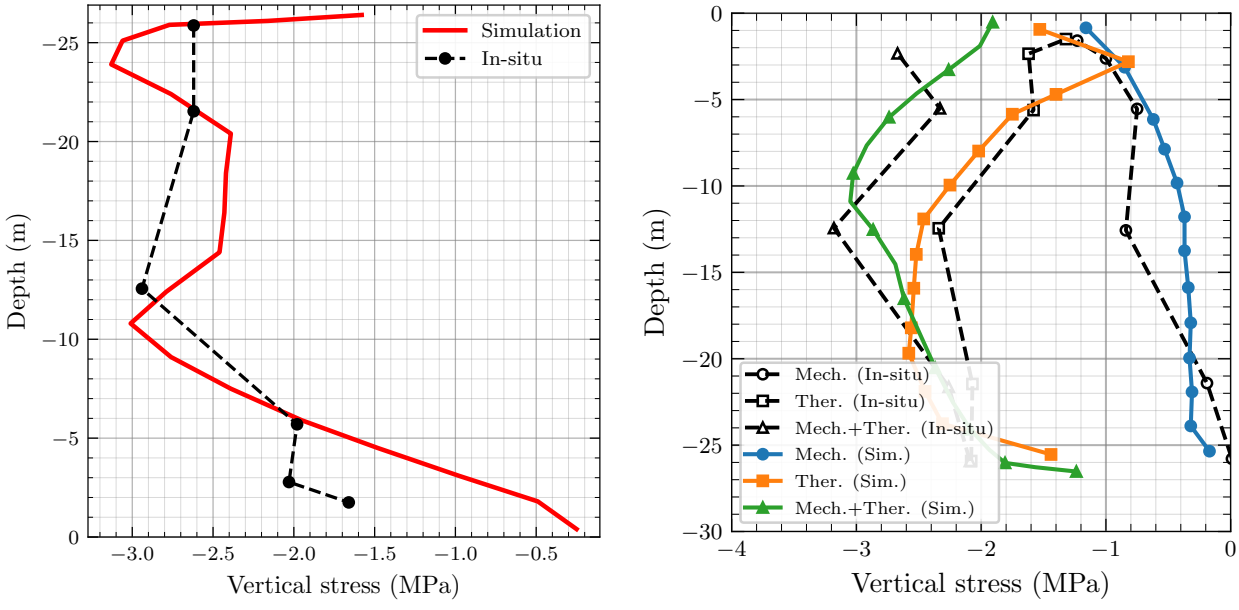


**FIGURE 8** (a) Comparison between measured and simulated thermal vertical stress distribution along the pile depth; (b) Comparison between measured and simulated thermomechanical vertical stress distribution along the pile depth.

The simulation results show good agreement with experimental data across all measured quantities: temperature distribution, axial and radial strain, vertical displacement, and induced stresses. The model effectively captures the coupled thermal and mechanical processes activated during geothermal operation and provides strong validation for the underlying elasto-viscoplastic interface formulation. The remaining minor deviations are attributed to idealized boundary conditions and simplified representation of heterogeneity in thermal and hydraulic properties.

## 5 | THERMALLY INDUCED EXCESS POREWATER PRESSURE

The generation of excess porewater pressure under thermal loading represents a fundamental mechanism governing the performance of energy piles in low-permeability soils. This phenomenon arises from the differential thermal expansion of the solid skeleton and pore fluid under constrained drainage conditions, leading to significant increases in porewater pressure that can substantially impact pile-soil interface behavior. To systematically investigate the coupled effects of soil hydraulic properties and thermal boundary conditions on porewater pressure evolution, a comprehensive parametric study was conducted using the enhanced thermo-hydro-mechanical (THM) framework developed in this investigation.

## 5.1 | Parametric investigation framework

The parametric study encompasses five orders of magnitude variation in soil permeability, ranging from $10^{-6}$ to $10^{-14}$ $m^2$, representing the spectrum from highly permeable sandy soils to extremely low-permeability clayey formations typical of energy pile installations. Four distinct fluid temperatures were investigated: 21°C (ambient baseline), 30°C, 40°C, and 50°C, corresponding to typical operational ranges for geothermal heat pump systems and extreme operational scenarios. For each permeability-temperature combination, interface nodes between the pile and surrounding soil were monitored continuously along the pile depth to capture the spatial and temporal evolution of porewater pressure fields.

The assumption of fully undrained heating conditions was rigorously maintained for low-permeability scenarios ($k < 10^{-10}$ $m^2$), consistent with field observations from geothermal pile installations in clayey strata where drainage time scales significantly exceed typical heating durations. This assumption is further validated by the work of Fuentes et al.[8], who demonstrated that for permeabilities below $k < 10^{-10}$ $m^2$, the characteristic time for porewater pressure dissipation exceeds several months, far longer than typical thermal loading cycles.

## 5.2 | Mechanisms of thermal pressurization

The thermal pressurization mechanisms in energy pile-soil interface are fundamentally governed by the coupled thermo-hydro-mechanical processes occurring within the zero-thickness interface elements that represent the pile-soil contact zone. The developed non-isothermal elasto-viscoplastic interface model provides a framework for calculating porewater pressure buildup with temperature increase through the simultaneous solution of mass balance, energy balance, and mechanical equilibrium equations at the interface.

The computational process starts from the water mass balance (Eq. 33), which sums storage and fluxes of water in both the liquid and vapour phases across the interface aperture, together with the companion air mass balance and energy balance equations. The water content terms $\theta_l^w$ and $\theta_g^w$ are inherently temperature-dependent, capturing the thermal expansion characteristics of each phase within the constrained geometry of the zero-thickness interface element. As temperature increases, the differential expansion between the pore fluid (with thermal expansion coefficient $\beta_w \approx 3.4 \times 10^{-4}$ °$C^{-1}$) and the interface zone creates volumetric incompatibility that cannot be accommodated through elastic deformation alone. The interface aperture $e$ plays a critical role in controlling this process, as it defines the effective volume available for fluid expansion and directly influences the magnitude of pressure generation.

The framework calculates excess porewater pressure through the coupled solution of the mass and energy balance equations, where temperature $T$ appears as a primary unknown alongside liquid and gas pressures ($p_l$, $p_g$) and interface displacements ($\delta_{n,T}$, $\delta_{s,T}$). This coupling is essential because the energy balance equation (Eq. 37) reveals that the specific internal energies $E_l^w$ and $E_g^w$ for water in liquid and gas phases are temperature-dependent, creating direct feedback between thermal and hydraulic processes. The advective energy fluxes $[j_{E_l}]$ and $[j_{E_g}]$ represent the transport of thermal energy through fluid movement, establishing spatial variations in temperature that drive localized pressure changes throughout the interface zone.

The mechanical response of the interface controls porewater pressure via the temperature-dependent normal and tangential stiffness. According to Eq. (8), heating induces softening, and once $\dot{\delta}_n^{vp}$ exceeds $\left(\dot{\delta}_{n,T}^{vp}\right)_{\text{tr}}$, thermal softening accelerates normal closure, reducing the aperture $e$. The loss of $e$ lowers storage and, more critically, transmissivity ( $\propto e^3$ ), which limits drainage and amplifies thermal pressurization. This mechano-hydraulic coupling is strongest when the interface is under compression and closure dominates. This temperature-induced stiffness reduction amplifies the thermal pressurization effect, creating a mechanical-hydraulic coupling that becomes particularly pronounced when the viscoplastic displacement rate exceeds the threshold value $\left(\dot{\delta}_{n,T}^{vp}\right)_{\text{tr}}$, triggering thermal softening and enhanced pressure buildup.

The non-isothermal elasto-viscoplastic law can amplify thermal pressurization when slip causes net normal closure. In $f_T$, the temperature- and slip-dependent strength parameters $c_T$ and $\phi_T$ (Eqs. 12-13) degrade with heating and accumulated slip, promoting additional viscoplastic slip at a given shear traction. With a small/negative dilation angle, slip reduces the aperture $e$, lowering storage and transmissivity ( $\propto e^3$ ) and thus limiting drainage. Under heating, this contraction enhances porewater pressure buildup. The result is a feedback: thermal pressurization promotes slip; slip contracts the interface; reduced $e$ intensifies pressurization. This creates a computational feedback loop where thermal pressurization promotes slip, which in turn accelerates strength degradation and further amplifies pressure buildup.

The framework calculates the direct impact of thermal pressurization on interface performance through the effective stress relationship (Eq. 4), where the porewater pressures $p_{g,mp}$ and $p_{l,mp}$ are determined by the coupled solution of the THM balance equations. As thermal pressurization increases these porewater pressures, the effective stress decreases, leading to reduced interface shear capacity according to the temperature-dependent strength envelope (Eq. 11). This reduction in effective stress and shear capacity represents the fundamental computational mechanism by which the framework quantifies how thermal pressurization degrades pile shaft resistance in energy pile systems.

The temporal evolution of thermal pressurization is controlled computationally through the balance between pressure generation and dissipation mechanisms captured in the mass balance equations. The transverse and longitudinal flux components ($q_l^{\perp}$, $q_l^{\parallel}$, $q_g^{\perp}$, $q_g^{\parallel}$) govern the drainage capacity of the interface zone, while the non-advective flux terms ($i_{lt}^w$, $i_{ll}^w$, $i_{gt}^w$, $i_{gl}^w$) represent diffusive transport processes that provide alternative pathways for pressure dissipation. In low-permeability conditions typical of stiff clays, the limited drainage capacity restricts the dissipation of thermally generated excess pressures, leading to sustained pressure elevation and prolonged effective stress reduction. The interface aperture $e$ and length $L_e$ parameters in the mass balance equations control the effective volume available for pressure dissipation, making the geometric characteristics of the interface zone critical computational factors in determining the magnitude and persistence of thermal pressurization effects.

The computational framework thus provides a comprehensive approach for calculating porewater pressure buildup by simultaneously solving the coupled system of equations that govern thermal expansion, mechanical deformation, and fluid flow at the pile-soil interface. The temperature-dependent material properties, viscoplastic slip mechanisms, and drainage characteristics are all integrated within the solution process, enabling accurate prediction of thermal pressurization effects under realistic operational conditions for energy pile systems.

## 5.3 | Analysis of pressure evolution

The simulation results presented in Figure 9 demonstrate the fundamental relationship between soil permeability, operating temperature, and thermal pressurization in the energy pile–soil interface. Figure 9a reveals a systematic logarithmic relationship between permeability and excess Porewater pressure accumulation, with each order of magnitude reduction in permeability producing progressively higher pressure buildup across all temperature conditions. The data clearly identify two critical permeability thresholds that govern thermal pressurization behavior. The first critical threshold occurs at $k = 10^{-9}$ m², marking a transition from moderate to severe thermal pressurization conditions. Below this threshold, thermal pressurization intensifies dramatically, establishing this permeability value as a fundamental design boundary. A second critical threshold emerges at $k = 10^{-11}$ m², representing a severe risk boundary where thermal effects become extreme across all operating temperatures.

The temperature effect is evident through the discrete data points representing four operational conditions: 21°C (baseline), 30°C, 40°C, and 50°C. For any given permeability, increasing temperature systematically elevates excess porewater pressure generation, with the 50°C condition consistently producing the highest pressures across the entire permeability range. The temperature-dependent response exhibits consistent patterns across all permeability conditions, indicating predictable thermal scaling behavior. The secondary y-axis in Figure 9a presents the effective stress ratio $\Delta u/\sigma'_{v0}$, providing direct quantification of thermal effects on soil effective stress. This ratio represents the fraction of initial effective stress affected by thermal pressurization, with values approaching 0.5 indicating significant effective stress reduction and values reaching 1.0 representing complete effective stress loss. The purple data points overlaid on the secondary axis demonstrate the spatial distribution of these effects throughout the pile length. Horizontal reference lines at ratios of 0.5 and 1.0 provide clear visual indicators, enabling rapid assessment of thermal impact severity.

The depth-segmented analysis presented in Figure 9 reveals distinct thermal pressurization patterns across three depth zones. The shallow zone (0-10m) analysis in Figure 9b shows the lowest pressure accumulation across all permeability-temperature combinations, reflecting enhanced drainage efficiency near the ground surface. The intermediate zone (10-20m) analysis in Figure 9c demonstrates elevated pressure buildup compared to the shallow zone, indicating reduced drainage effectiveness with depth. The deep zone (20-26m) analysis in Figure 9d exhibits the most severe thermal pressurization conditions, with the highest pressure accumulation occurring at the pile tip region, where thermal loading effects are most pronounced. Each depth-segmented subplot maintains the same permeability range and temperature conditions as the main plot, allowing for a direct comparison of thermal effects across different pile depths. The consistent data patterns across all three depth zones confirm that the fundamental permeability-controlled behavior remains valid throughout the pile length, while the absolute pressure magnitudes vary systematically with depth position.

The color coding in all figures represents normalized depth position along the pile, providing additional spatial context for the thermal pressurization analysis. This comprehensive visualization enables the simultaneous assessment of permeability effects, temperature dependencies, effective stress impacts, and depth-related variations within a single, integrated analysis framework.

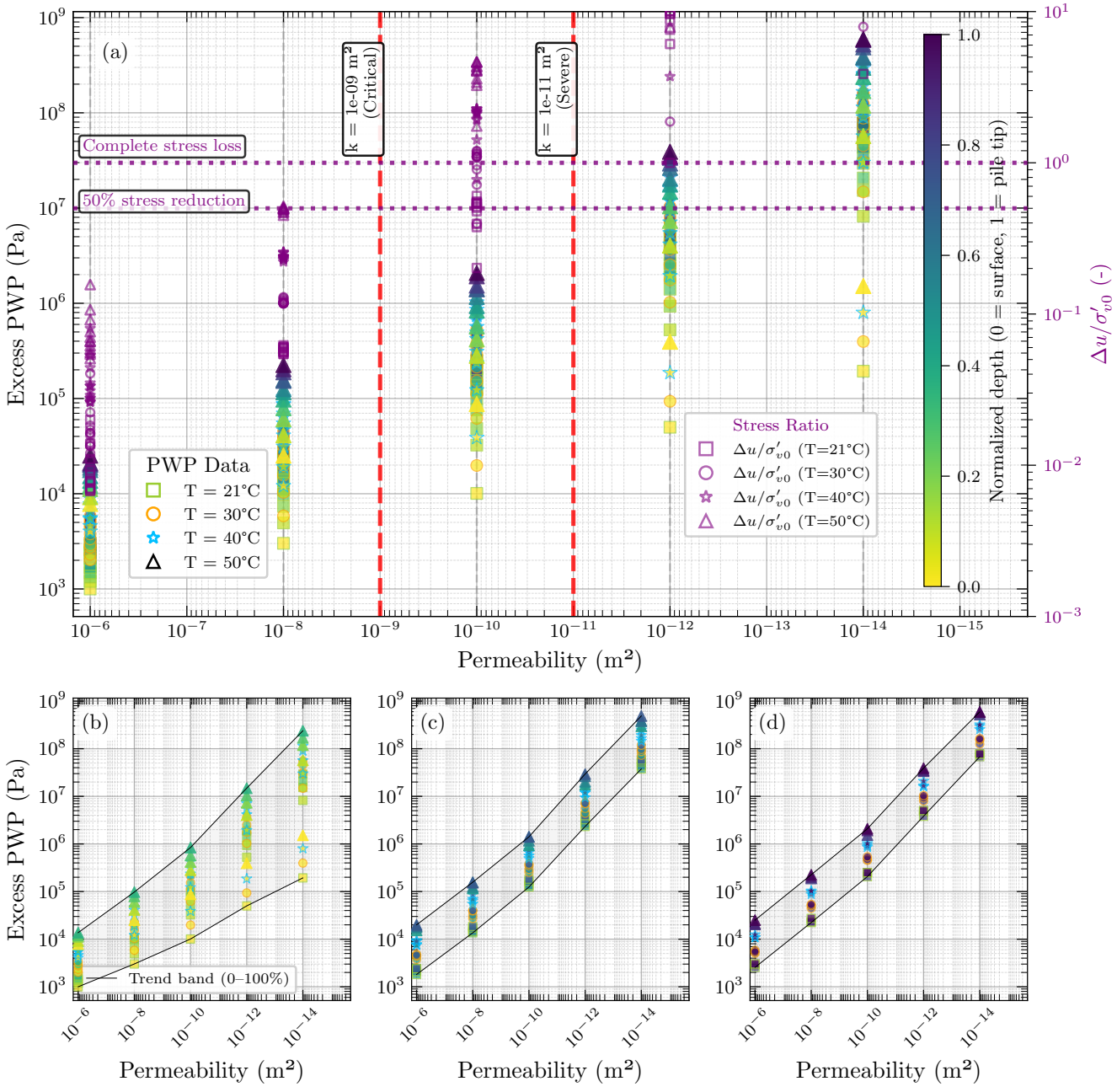


**FIGURE 9** The relationship between soil permeability, operating temperature, and thermal pressurization. (a) excess porewater pressure versus permeability with temperature data points and critical threshold annotations. The secondary y-axis shows the effective stress ratio $\Delta u/\sigma'_{v0}$. (b) depth-segmented analysis for shallow (0-10m); (c) intermediate (10-20m); and (d) deep (20-26m) zones. Color coding indicates normalized depth position along the pile.

## 5.4 | Spatial pressure development

The depth profile analysis in Figure 10 shows the spatial distribution of thermal effects along the pile length for four operational scenarios: low permeability with high temperature (LP-HT, $k = 10^{-12}$ m$^2$, $T = 50$°C), low permeability with moderate temperature (LP-MT, $k = 10^{-12}$ m$^2$, $T = 30$°C), moderate permeability with high temperature (MP-HT, $k = 10^{-10}$ m$^2$, $T = 50$°C), and high permeability with high temperature (HP-HT, $k = 10^{-8}$ m$^2$, $T = 50$°C). The initial effective stress profile (Figure 10a) shows the baseline geotechnical conditions across four soil layers: alluvial soils $A_1$ (0-5m) and $A_2$ (5-10m), sandy gravelly moraine B (10-22m), and bottom moraine C (22-26m). The effective stress increases from 2.1 MPa at the surface to 2.6 MPa at 26m depth, with distinct changes in gradient at layer boundaries reflecting the different unit weights of each geological unit.

The excess porewater pressure profiles (Figure 10b) demonstrate systematic thermal pressurization across the operational scenarios. The LP-HT scenario produces the highest pressures, ranging from 270 kPa at the surface to 405 kPa at the pile tip. The LP-MT scenario shows reduced pressures (84-126 kPa) due to lower temperature increase. The MP-HT and HP-HT scenarios exhibit progressively lower pressures (180-270 kPa and 72-108 kPa, respectively) due to enhanced drainage at higher permeabilities. All profiles show increasing pressure with depth, reflecting more confined conditions and reduced drainage efficiency at greater depths.

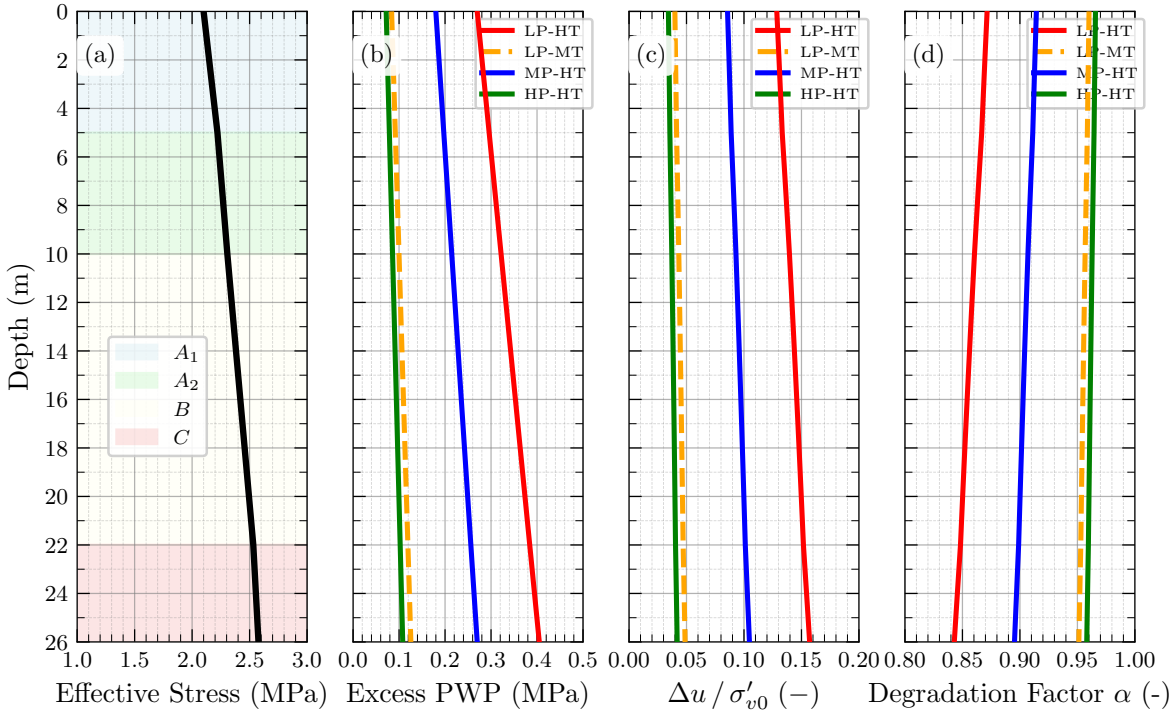


**FIGURE 10** Depth profile analysis showing the spatial distribution of thermal effects along the pile length. (a) initial effective stress profile with soil layer stratification; (b) excess porewater pressure profiles for different permeability-temperature scenarios; (c) effective stress reduction ratios ($\Delta u/\sigma'_{v0}$), and (d) degradation factor profiles.

The effective stress reduction ratios (Figure 10c) quantify the relative magnitude of thermal effects. The LP-HT scenario produces ratios of 0.13-0.16, indicating that thermal pressurization reduces the effective stress by 13-16%. The LP-MT scenario shows smaller ratios (0.04-0.05), while the MP-HT and HP-HT scenarios produce intermediate and minimal ratios (0.09-0.11 and 0.03-0.04, respectively). These ratios remain below 0.20 for all examined conditions, indicating moderate thermal effects that preserve substantial effective stress for shaft resistance mobilization. The degradation factor profiles (Figure 10d) translate stress ratios into shaft capacity reduction. The LP-HT scenario shows degradation factors of 0.84-0.87, indicating 13-16% shaft capacity loss. The LP-MT scenario maintains factors of 0.95-0.96 (4-5% loss), while MP-HT and HP-HT scenarios show 9-11%

and 3-4% capacity losses, respectively. All scenarios maintain degradation factors above 0.84, confirming that the pile retains at least 84% of its original shaft capacity under the examined thermal loading conditions.

The comparative analysis reveals a clear hierarchy: LP-HT > LP-MT > MP-HT > HP-HT, demonstrating that both reduced permeability and increased temperature contribute to enhanced thermal pressurization. The soil layer transitions are visible in all profiles, with gradient changes at boundaries reflecting the influence of geological stratification on thermal response. These results provide a quantitative foundation for energy pile design, showing that moderate thermal effects can be expected under typical operational conditions, with capacity reductions generally remaining below 20% for the parameter ranges examined.

## 5.5 | Time-dependent pressure and stress evolution

The temporal analysis presented in Figure 11 reveals time-dependent thermal pressurization mechanisms that exhibit distinct permeability-controlled evolution patterns, asymmetric heating-cooling dynamics, and persistent thermal effects that challenge conventional assumptions about thermal loading reversibility.

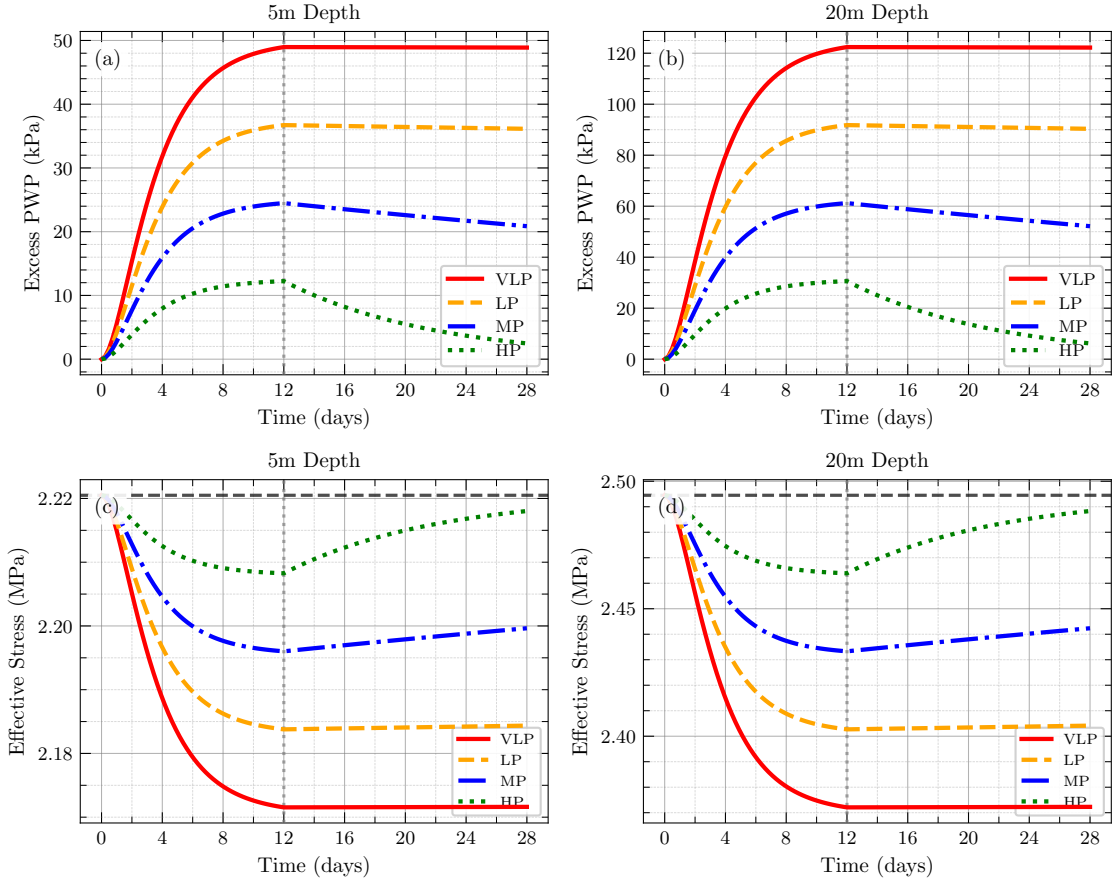


Legend: VLP = Very Low Permeability ($k = 1 \times 10^{-12}\,\mathrm{m}^2$); LP = Low Permeability ($k = 1 \times 10^{-11}\,\mathrm{m}^2$); MP = Moderate Permeability ($k = 1 \times 10^{-10}\,\mathrm{m}^2$); HP = High Permeability ($k = 1 \times 10^{-9}\,\mathrm{m}^2$). PWP = Pore Water Pressure. Heating phase: 0–12 days; Cooling phase: 12–28 days. Gray vertical line marks heating-cooling transition. Dashed black horizontal lines in (c) and (d) represent initial effective stress at each depth before any thermal loading.

**FIGURE 11** Time-dependent evolution of thermal effects during heating (0-12 days) and cooling (12-28 days) cycles. (a,b) Excess porewater pressure development at 5m and 20m depths showing permeability-dependent amplification and asymmetric recovery patterns; (c,d) effective stress evolution at 5m and 20m depths with black dashed lines indicating initial stress conditions. Gray vertical lines mark the heating-cooling transition at 12 days.

The excess porewater pressure evolution at shallow depth (Figure 11a) and deep depth (Figure 11b) reveals systematic permeability-dependent amplification patterns with consistent 2.5× depth amplification factors across all scenarios. Very low permeability conditions (VLP, $k = 10^{-12}$ m$^2$) produce maximum pressures of 49.0 kPa (shallow) and 122.4 kPa (deep), representing the most severe thermal pressurization scenario. The pressure evolution demonstrates an exponential approach during heating with time constants of 3.9 days, followed by different cooling behavior where pressure dissipation rates span four orders of magnitude: from 6.9 days (HP) to 6,931 days (VLP).

The effective stress evolution at shallow depth (Figure 11c) and deep depth (Figure 11d) demonstrates the direct effect of thermal pressurization on soil strength. During thermal loading, effective stress reductions follow the inverse pattern of porewater pressure development, with VLP conditions showing maximum stress reductions of 0.049 MPa (shallow) and 0.122 MPa (deep). The temporal analysis reveals a critical asymmetry in stress recovery, with VLP conditions showing only 0.2% pressure recovery during the 16-day cooling phase compared to 79.8% recovery for HP conditions. This finding establishes that effective stress degradation in low-permeability soils exhibits quasi-permanent characteristics that accumulate over multiple thermal cycles.

The depth amplification phenomenon is clearly demonstrated through the comparative analysis between shallow and deep locations. Maximum porewater pressures increase by 2.5× from 5m to 20m depth across all permeability scenarios, while effective stress reductions show proportional amplification. This systematic depth dependency indicates that thermal effects become progressively more severe with depth, with the pile tip experiencing the most significant thermal loading. The consistent amplification factor across different permeability conditions suggests that depth effects are primarily controlled by thermal and hydraulic mechanisms rather than soil-specific properties.

The permeability-dependent recovery characteristics reveal fundamental differences in the reversibility of thermal loading. High permeability conditions demonstrate rapid pressure dissipation and effective stress recovery, with both parameters returning to near-baseline conditions within the 16-day cooling period. Conversely, very low permeability conditions show minimal recovery, with porewater pressures and effective stress reductions persisting at elevated levels throughout the cooling phase. This asymmetric behavior creates conditions that allow multiple thermal cycles to produce cumulative degradation effects in low-permeability soils.

## 6 | SHAFT RESISTANCE DEGRADATION

Thermal cycles in geothermal piles lead to coupled thermo–hydro–mechanical processes at the pile-soil interface. As detailed in the non-isothermal elasto–viscoplastic formulation (Section 2), temperature changes not only alter the stiffness of the interface but also generate excess porewater pressures and modify the intrinsic strength parameters. These combined effects reduce the mobilized shear stress along the pile shaft and must therefore be quantified in design.

Following the framework proposed by Fuentes et al.[8], the effect of thermally induced excess porewater pressures can be expressed through a shaft resistance reduction ratio. This dimensionless parameter quantifies the degradation of interface shear strength under non-isothermal conditions relative to isothermal reference conditions. The shaft resistance reduction ratio is defined as

$$R_\tau = \frac{\tau_{w/\text{temp}}}{\tau_{wo/\text{temp}}} \tag{41}$$

where $\tau_{w/\text{temp}}$ is the shear stress at the pile–soil interface with temperature changes and $\tau_{wo/\text{temp}}$ is the shear stress without temperature effects.

The shear stress at the interface can be generally written in terms of the effective normal stress as $\tau = \sigma'_n \tan\varphi'$, which can be developed into

$$\tau = K_m \sigma'_v \tan\varphi' \tag{42}$$

where $K_m$ is a mobilized earth pressure coefficient at the interface and $\sigma'_v$ is the vertical effective stress. For the case with temperature changes, the vertical effective stress is reduced by thermally induced excess porewater pressure. Writing the vertical effective stress as a function of total and porewater pressures gives

$$\tau_{w/\text{temp}} = K_m(\sigma_v - u_0 - \Delta u)\tan\varphi' \tag{43}$$

where $u_0$ is the initial porewater pressure before temperature changes are applied, and $\Delta u$ is the thermally induced excess porewater pressure. The same formulation for the case without temperature is

$$\tau_{wo/\text{temp}} = K_m(\sigma_v - u_0)\tan\varphi' \tag{44}$$

Substituting Eqs. (43) and (44) into Eq. (41), and assuming that $K_m$ and $\tan\varphi'$ do not change when the temperature gradient is applied, gives the most general form of the shaft resistance reduction ratio

$$R_\tau = \frac{\sigma_v - u_0 - \Delta u}{\sigma_v - u_0} \tag{45}$$

or equivalently

$$R_\tau = 1 - \frac{\Delta u}{\sigma_v - u_0}. \tag{46}$$

The independence of $K_m$ and $\tan\varphi'$ to temperature gradients was demonstrated by[32], who showed that the strain and total stress changes at the interface are small when the temperature is applied. The shaft resistance reduction ratio $R_\tau$ is bound between negative values and 1.0, where $R_\tau = 1.0$ when there is no thermal loading (i.e., $\Delta u = 0$), $R_\tau = 0$ if $\Delta u = \sigma_v - u_0$ (complete loss of effective stress), and $R_\tau < 0$ when $\Delta u > \sigma_v - u_0$ (excess porewater pressure exceeds initial effective stress).

For saturated soils where the water table is at the ground surface and the vertical planes are principal planes, $\sigma_v = \gamma_{\text{sat}} z$ and $\sigma_v - u_0 = \gamma' z$. Under these conditions, Eq. (45) can be rewritten as

$$R_\tau = 1 - \frac{\Delta u}{\gamma' z}. \tag{47}$$

This formulation highlights that the shaft resistance reduction ratio depends on the magnitude of thermally induced excess porewater pressure $\Delta u$, the initial effective stress state $\sigma'_{v0} = \sigma_v - u_0$, and the depth $z$ along the pile shaft.

For practical design applications, it is convenient to define a degradation factor $\alpha$ that represents the remaining shaft capacity under thermal loading as

$$\alpha = R_\tau = 1 - \frac{\Delta u}{\sigma'_{v0}}. \tag{48}$$

This degradation factor is bound between negative values and 1, where $\alpha = 1$ indicates no degradation and $\alpha = 0$ indicates complete loss of shaft resistance. The total shaft capacity under thermal loading can then be expressed as

$$Q_{s,T} = \int_0^L \alpha(z,t) \cdot f_{s,0}(z) \cdot P \, \mathrm{d}z \tag{49}$$

where $L$ is the pile length, $f_{s,0}(z)$ is the unit shaft resistance under isothermal conditions, and $P$ is the pile perimeter.

The magnitude of the degradation factor $\alpha$ is primarily controlled by soil permeability, soil compressibility, temperature increase, depth, and drainage conditions. Low-permeability soils ($k < 10^{-11}$ m/s) experience limited drainage during thermal loading, leading to higher excess porewater pressures and greater shaft resistance reduction, while high-permeability soils allow rapid dissipation of thermal pressures, resulting in minimal degradation. Stiffer soils with lower compressibility generate higher thermal pressures for a given temperature change, as the volumetric expansion of porewater is more constrained, whereas compressible soils accommodate thermal expansion more readily, reducing pressure buildup. Higher temperature increases produce proportionally larger thermal expansion of porewater, resulting in greater excess pore pressures and more significant shaft resistance degradation. The degradation effect is more pronounced at shallow depths where the initial effective stress is lower; at greater depths, the same excess porewater pressure represents a smaller fraction of the total effective stress, resulting in less relative degradation. Rapid thermal loading or cyclic heating without sufficient rest periods prevents full dissipation of excess pressures, leading to cumulative degradation over multiple cycles, while slow heating rates allow partial drainage, reducing the peak thermal pressures.

The shaft resistance reduction ratio provides a rational framework for assessing thermal effects on geothermal pile capacity. In numerical simulations, the excess porewater pressure $\Delta u(z,t)$ is directly computed at each time step from the coupled THM analysis, allowing straightforward evaluation of the degradation factor through Eq. (48). For design purposes, conservative estimates of $\alpha$ should account for the most critical combination of low permeability, high temperature increase, and shallow depth.

## 6.1 | Shaft resistance degradation analysis

The degradation factor analysis presented in Figure 12 reveals fundamental permeability-controlled mechanisms governing thermal effects on energy pile capacity. The comprehensive analysis demonstrates that thermal degradation exhibits distinct

behavioral regimes characterized by critical permeability thresholds rather than continuous transitions, establishing quantitative boundaries for thermal loading assessment in energy pile design.

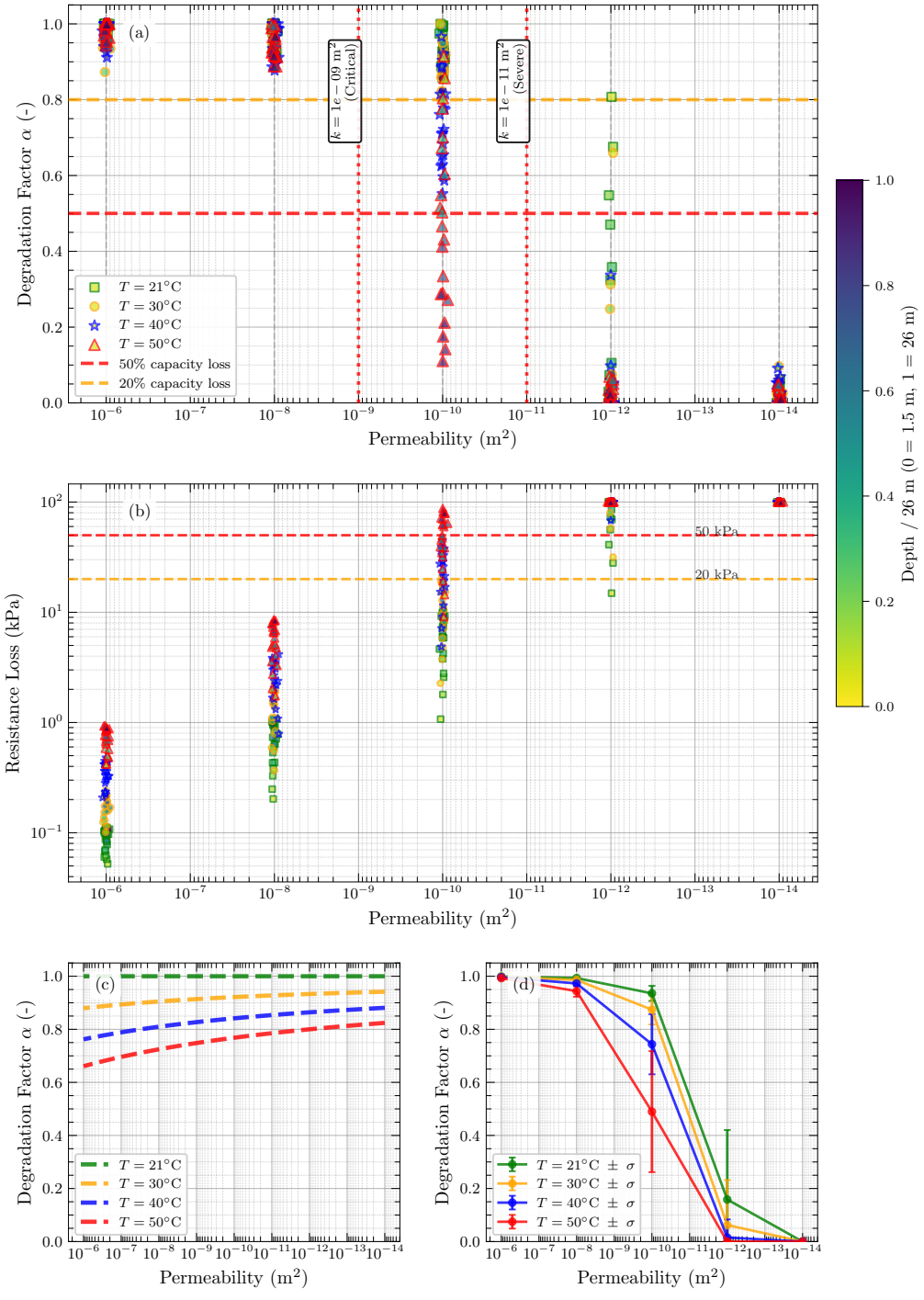


**FIGURE 12** Comprehensive shaft resistance degradation analysis showing (a) degradation factor versus permeability with critical thresholds, (b) absolute resistance loss quantification, (c) theoretical degradation curves based on empirical relationship, and (d) Depth-averaged degradation factor with spatial variability. Color coding indicates normalized depth position along the pile.

The degradation factor evolution (Figure 12a) reveals three distinct performance regimes defined by permeability boundaries. High-permeability conditions ($k > 10^{-9}$ m$^2$) maintain degradation factors above $\alpha = 0.9$, indicating minimal thermal impact with less than 10% capacity reduction. The critical transition occurs at $k = 10^{-11}$ m$^2$, where degradation factors drop precipitously to the $\alpha = 0.5$-$0.8$ range, representing 20-50% shaft capacity loss. Below $k = 10^{-12}$ m$^2$, severe degradation conditions emerge with degradation factors approaching zero ($\alpha < 0.1$), indicating near-complete loss of shaft resistance under thermal loading.

Temperature scaling effects demonstrate systematic amplification patterns with degradation intensifying approximately 2-fold per 10 °C increase across all permeability ranges. This scaling relationship provides quantitative basis for operational temperature limit establishment, with the most pronounced effects occurring in low-permeability conditions where temperature restrictions become critical design constraints. The depth dependency, visualized through color coding, reveals progressive degradation intensification from shallow (green) to deep (purple) locations, with intermediate depths showing 5-fold greater degradation than surface conditions.

The absolute resistance loss quantification (Figure 12b) provides direct engineering metrics for design application, demonstrating resistance losses ranging from negligible values in permeable soils to complete capacity elimination in impermeable conditions. The logarithmic scaling reveals that 47.6% of evaluated scenarios exceed the 20% capacity loss threshold, while 41.4% experience severe degradation with greater than 50% capacity reduction, establishing the prevalence of significant thermal effects across realistic soil conditions.

The theoretical prediction framework (Figure 12c) demonstrates that degradation behavior follows exponential decay relationships with respect to both permeability and temperature, enabling predictive modeling for design applications. The temperature-dependent curves capture the fundamental physics of thermal pressurization, with steeper decay rates at higher temperatures reflecting intensified thermal loading effects.

Figure 12d presents the mean degradation factor and its spatial variation (±1 standard deviation) along the pile depth for each permeability–temperature combination. The error bars quantify the depth-dependent variability of $\alpha$, which arises from the increasing effective stress with depth according to Eq. (48). Greater variability occurs in intermediate permeability ranges ($10^{-11}$ to $10^{-10}$ m$^2$), where the degradation is most sensitive to the competing effects of thermal pressurization and drainage capacity.

Critical design implications emerge from the permeability threshold identification, establishing $k = 10^{-11}$ m$^2$ as the fundamental boundary where thermal effects transition from manageable to critical. This threshold provides quantitative guidance for site characterization requirements and thermal loading assessment protocols. The 14-fold amplification factor between $k = 10^{-10}$ and $k = 10^{-12}$ m$^2$ conditions demonstrates the extreme sensitivity of thermal effects to permeability variations, necessitating precise soil characterization in the critical permeability range for reliable thermal loading prediction.

## 6.2 | Shaft capacity evolution

The temporal analysis of shaft capacity evolution presented in Figure 13 reveals permeability-dependent thermal loading effects with different time constants for heating and cooling phases. The shaft capacity evolution demonstrates that thermal effects exhibit distinct heating-cooling dynamics, establishing critical design considerations for long-term energy pile performance under operational loading.

The depth-averaged shaft capacity loss analysis demonstrates permeability-controlled degradation patterns with maximum losses ranging from 0.55% (HP) to 5.5% (VLP) during peak thermal loading. The temporal evolution exhibits rapid capacity loss during the 12-day heating phase, characterized by exponential approach to maximum degradation with time constants of approximately 3.9 days across all permeability scenarios. This rapid response reflects the immediate development of thermal pressurization as heating progresses, with shaft capacity reduction following the temperature evolution pattern established in the thermal boundary condition.

Different recovery behavior emerges during the 16-day cooling phase, where shaft capacity recovery demonstrates extreme permeability dependence. High-permeability conditions (HP) achieve substantial recovery of 0.44 percentage points (79.8% of initial loss), returning to near-baseline shaft capacity levels within the cooling period. Conversely, very low permeability conditions (VLP) show virtually no recovery, with shaft capacity remaining at degraded levels throughout the cooling phase. This behavior creates a 1,000× ratio between heating and cooling time constants for VLP conditions, indicating fundamental irreversibility in thermal loading effects for low-permeability soils.

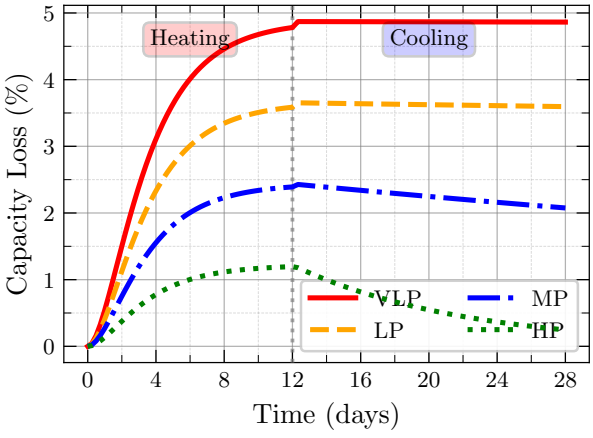


**FIGURE 13** Depth-averaged shaft capacity loss (percentage of initial shaft capacity) during 12-day heating and 16-day cooling cycle, showing permeability-dependent degradation and limited recovery in low-permeability conditions. VLP = Very Low Permeability ($k = 1 \times 10^{-12}$ m$^2$); LP = Low Permeability ($k = 1 \times 10^{-11}$ m$^2$); MP = Moderate Permeability ($k = 1 \times 10^{-10}$ m$^2$); HP = High Permeability ($k = 1 \times 10^{-9}$ m$^2$).

## 6.3 | Engineering implications and design considerations

The operational temperature guidelines (Figure 14a) establish quantitative boundaries based on acceptable depth-averaged shaft capacity degradation levels, revealing critical design thresholds that vary by four orders of magnitude across the permeability spectrum. For high-permeability conditions ($k > 10^{-9}$ m$^2$), operational temperatures up to 60 °C produce negligible thermal effects, enabling unrestricted energy pile operation. However, the analysis identifies a critical permeability threshold at $k = 10^{-11}$ m$^2$ where allowable temperatures decrease dramatically: from 45 °C to 25 °C for depth-averaged shaft capacity loss thresholds of 20% and 10%, respectively. This threshold represents a fundamental design boundary where thermal effects transition from manageable to potentially critical, necessitating site-specific thermal loading assessment and operational constraint development.

The degradation factor contours (Figure 14b) provide a comprehensive design tool for evaluating thermal effects across the full operational parameter space, enabling direct assessment of shaft capacity degradation for any combination of soil permeability and operating temperature. The contour map reveals the nonlinear coupling between permeability and temperature effects, with degradation factors ranging from $\alpha = 0.9$ (minimal thermal effects) to $\alpha = 0.1$ (severe degradation) depending on site conditions. This visualization enables designers to rapidly assess whether proposed operational parameters fall within acceptable performance limits or require design modifications.

The depth-dependent degradation factors (Figure 14c) illustrate the influence of depth on thermal degradation for a reference case of T = 30 °C. Each curve represents the degradation factor $\alpha$ at a specific depth (5, 10, 15, 20, or 25 m) as a function of soil permeability. The analysis demonstrates that deeper sections experience progressively greater degradation than shallow sections, with degradation factors decreasing from $\alpha = 0.95$ at 5m depth to $\alpha = 0.81$ at 25m depth for intermediate permeability conditions ($k = 10^{-10}$ m$^2$). This depth stratification reflects the increasing thermal pore pressure generation with depth, which outpaces the compensating effect of increasing confining stress. The permeability dependence is most pronounced in the range $10^{-12}$ to $10^{-10}$ m$^2$, where degradation factors transition from near-unity (minimal thermal effects) to values approaching or below the 20% shaft capacity loss threshold ($\alpha = 0.8$). At very low permeability ($k < 10^{-12}$ m$^2$), all depth levels experience severe degradation, with deeper sections exceeding the 20% loss threshold and approaching 50% shaft capacity loss ($\alpha = 0.5$) at the pile tip.

The risk classification framework (Figure 14d) provides preliminary guidance for design approach selection based on soil permeability and operating temperature. The four-tier system categorizes conditions as: Low Risk ($k > 10^{-9}$ m$^2$, standard design procedures applicable), Moderate Risk ($10^{-11} < k < 10^{-9}$ m$^2$ with T < 35 °C, thermal considerations required), High Risk ($10^{-12} < k < 10^{-11}$ m$^2$, detailed thermal analysis necessary), and Very High Risk ($k < 10^{-12}$ m$^2$ with T > 35 °C, design modifications or operational constraints required). It must be emphasized that these risk categories represent illustrative thresholds for preliminary screening and must be adapted to project-specific requirements, including the relative contribution of shaft versus base capacity, applied safety factors, and acceptable performance criteria. The classification assumes a shaft-dominated pile in relatively

homogeneous soil conditions; site-specific analysis is required for stratified profiles or piles with significant base capacity contributions. The stepwise boundaries between risk zones, while useful for initial assessment, represent simplified thresholds applied to the continuous degradation behavior shown in Figure 14b, and designers should recognize that actual risk transitions occur gradually rather than abruptly.

The integrated design framework establishes critical engineering implications that fundamentally alter energy pile design practice in low-permeability conditions. Enhanced site characterization with detailed permeability assessment is essential to identify conditions approaching the critical $10^{-11}$ m$^2$ threshold, as thermal effects become increasingly significant below this value. Operational temperature limits must be established based on site-specific soil conditions rather than generic constraints, utilizing the design charts to evaluate acceptable temperature ranges for measured permeability values. Current design approaches that neglect thermal effects or apply uniform degradation factors significantly underestimate capacity loss in low-permeability conditions, where quasi-permanent thermal effects require consideration of cumulative loading over the entire operational lifetime rather than cyclic assessment. For very low permeability conditions ($k < 10^{-12}$ m$^2$), the analysis demonstrates that thermal effects exhibit minimal recovery between heating cycles, necessitating integration of thermal-mechanical analysis into standard design procedures and potentially requiring operational constraints or enhanced pile dimensions to maintain adequate safety margins.

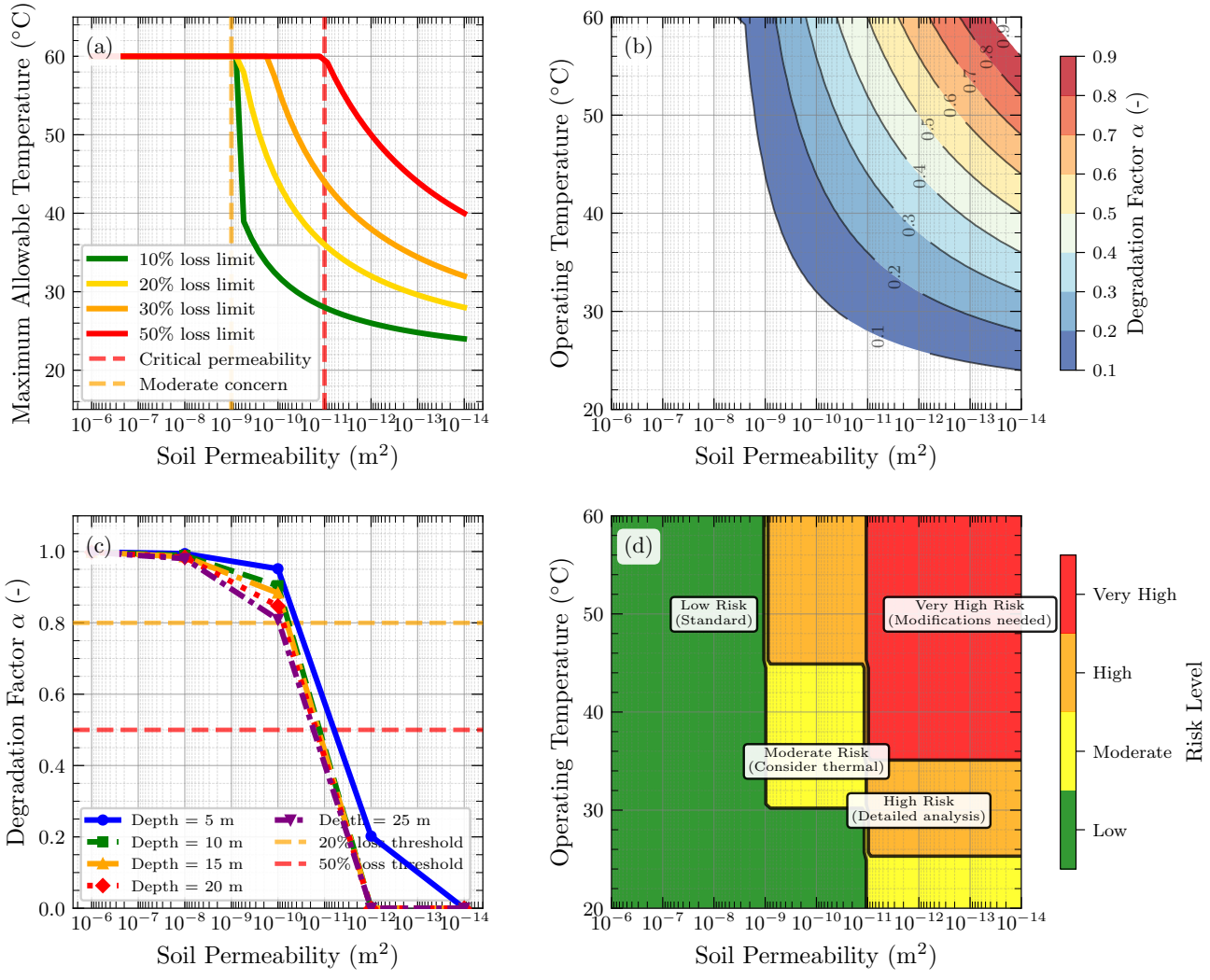


**FIGURE 14** Design charts for energy pile thermal loading assessment in low-permeability clays. (a) Maximum allowable operating temperature versus soil permeability for specified shaft capacity loss limits (10–50%); (b) degradation factor contours across operational parameter space; (c) depth-dependent degradation factors ($\alpha$) at T = 35 °C; (d) preliminary risk classification framework with four-tier system for design approach selection.

# 7 | CONCLUSIONS

This work examined the thermo–hydro–mechanical response of geothermal piles in low-permeability clays with a focus on interface behavior, excess porewater pressure generation, and the resulting reduction in mobilized shaft resistance under thermal activation. A zero-thickness thermo-viscoplastic interface formulation was generalized and implemented within a finite-element framework and compared with full-scale in-situ test observations. The simulations reproduce the expected coupled behavior by which heating generates excess porewater pressure at the interface, lowers effective normal stress, and diminishes shear transfer, while cooling partially reverses these effects with a clear path dependence due to viscoplasticity and hydraulic lag.

Permeability emerges as the controlling material parameter for both the amplitude and persistence of thermal pressurization. In the range characteristic of plastic clays, dissipation times are comparable to practical operational cycles, so strength recovery during cooling remains incomplete and a net seasonal reduction in available shaft resistance is observed. The proposed interface law captures temperature-dependent stiffness, rate-dependent inelastic slip, and the coupling between effective stress changes and shear mobilization, which proves necessary to represent the measured hysteresis and delayed strength recovery. Building on these mechanisms, a reduction function expressed in terms of temperature history and hydraulic diffusivity consistently bounds the simulated and observed loss of shaft resistance and is suitable for serviceability checks.

Comparisons against full-scale temperature fields, axial strains, and pile-head displacements show agreement in both timing and magnitude, indicating that the dominant mechanisms—thermal pressurization, effective-stress reduction, and interface softening—are correctly represented for the tested conditions. For design practice, explicitly accounting for thermal cycles in the assessment of shaft resistance is warranted in fine-grained soils. Operational envelopes that limit rapid or large temperature swings mitigate cumulative degradation, and drainage provisions that shorten dissipation times can materially improve performance without compromising energy yield.

The results demonstrate that explicit THM coupling at the pile–soil interface is essential for reliable prediction of energy-pile performance in clays, and that the presented constitutive framework and reduction function provide a tractable path to incorporate thermal cycling into routine design and assessment.

## ACKNOWLEDGMENTS

The authors acknowledge the financial support of the Luxembourg National Research Fund (FNR) for the EnergWALL project (grant FNR 18978786/ENERGWALL). The computational resources provided by the University of Luxembourg High-Performance Computing Facility are gratefully acknowledged.

## CONFLICT OF INTEREST

The authors declare no potential conflict of interests.

## REFERENCES

1. Brandl H. Energy foundations and other thermo-active ground structures. *Geotechnique.* 2006;56(2):81–122. doi: 10.1680/geot.2006.56.2.81
2. Johnston I, Narsilio G, Colls S. Emerging geothermal energy technologies. *KSCE Journal of Civil Engineering.* 2011;15(4):643–653.
3. Laloui L, Di Donna A. *Energy Geostructures: Innovation in Underground Engineering*. ISTE Ltd and John Wiley & Sons, 2013.
4. Bourne-Webb P, Burlon S, Javed S, Kürten S, Loveridge F. Analysis and design methods for energy geostructures. *Renewable and Sustainable Energy Reviews.* 2016;65:402–419.
5. Murphy K, McCartney JS. Seasonal response of energy foundations during building operation. *Geotechnical and Geological Engineering.* 2015;33(2):343–356.
6. Sutman M, Olgun CG, Laloui L. Cyclic load–transfer approach for the analysis of energy piles. *Journal of Geotechnical and Geoenvironmental Engineering.* 2019;145(1):04018101.
7. Cen D, Xia C. Review on heat transfer and thermo-mechanical behaviour of energy geostructures. *Underground Space.* 2025. doi: https://doi.org/10.1016/j.undsp.2025.06.003
8. Fuentes R, Pinyol N, Alonso E. Effect of temperature induced excess porewater pressures on the shaft bearing capacity of geothermal piles. *Geomechanics for Energy and the Environment.* 2016;8:30-37. Themed Issue on Selected Papers Symposium of Energy Geotechnics 2015 — Part IIdoi: https://doi.org/10.1016/j.gete.2016.10.003
9. Braun P, Delage P, Ghabezloo S, Chabot B, Conil N, Vu MN. Inducing tensile failure of claystone through thermal pressurization in a novel triaxial device. *Rock Mechanics and Rock Engineering.* 2022;55(7):3881–3899.
10. Hueckel T, Francois B, Laloui L. Explaining thermal failure in saturated clays. *Geotechnique.* 2009;59(3):197–212. doi: 10.1680/geot.2009.59.3.197
11. Delage P, Cui YJ, Sultan N. On the thermal behaviour of Boom clay. *Eurosafe 2004.* 2004;354:10.
12. Laloui L, Nuth M, Vulliet L. Experimental and numerical investigations of the behaviour of a heat exchanger pile. *International Journal for Numerical and Analytical Methods in Geomechanics.* 2006;30(8):763–781. doi: 10.1002/nag.499
13. Cui YJ, Yahia-Aissa M, Delage P. A model for the volume change behavior of heavily compacted swelling clays. *Engineering geology.* 2002;64(2-3):233–250.
14. Tourchi S, Loche M, Scaringi G, Ring Tc. Temperature-dependent residual shear strength of bentonite : experimental investigation and numerical modelling. 2023.

15. Abuel-Naga HM, Pender M, Bergado DT, Bouazza A. Thermomechanical model for saturated clays. *Géotechnique.* 2009;59(3):273–278. ISBN: 0016-8505\n1751-7656doi: 10.1680/geot.2009.59.3.273
16. Tang A, Cui Y, Pereira J. A micromechanical approach to the thermo-plastic behavior of clays. *Computers and Geotechnics.* 2016;72:122–131. doi: 10.1016/j.compgeo.2015.11.004
17. Belmokhtar M, Tang A, Pereira J, Cui Y. Temperature effects on the mechanical behavior of a natural stiff clay. *Engineering Geology.* 2018;239:76–86. doi: 10.1016/j.enggeo.2018.03.022
18. Bourne-Webb PJ, Amatya B, Soga K, Amis T, Davidson C, Payne P. Energy pile test at Lambeth College, London: Geotechnical and thermodynamic aspects of pile response to heat cycles. *Géotechnique.* 2009;59(3):237–248.
19. Yavari N, Tang AM, Pereira JM, Hassen G. Effect of temperature on the shear strength of soil–structure interface. *Canadian Geotechnical Journal.* 2016;53(7):1186–1194. doi: 10.1139/cgj-2015-0313
20. Ng CWW, Shi C, Gunawan A, Laloui L. Centrifuge modelling of energy piles subjected to heating and cooling cycles in clay. *Géotechnique Letters.* 2014;4(4):310–316. doi: 10.1680/geolett.14.00063
21. Mohanto S, Singh K, Chakraborty T, Basu D. Cyclic thermo-mechanical analysis of wellbore in underground compressed air energy storage cavern. *Geotechnical and Geological Engineering.* 2014;32(3):601–616.
22. Bandeira Neto LA, Fei W, Narsilio GA. Improving thermal performance of groups of energy screw piles with phase change materials. *Applied Thermal Engineering.* 2024;236:121874. doi: https://doi.org/10.1016/j.applthermaleng.2023.121874
23. Magdy A, Rezaei M, Karami M. A review of exploiting shallow geothermal energy through tunnels: Current status and future prospects. *Renewable Energy.* 2025;238:1001–1023. doi: 10.1016/j.renene.2024.12.108
24. Hamidi A, Shirash A, Tourchi S. On the thermal failure of sand-clay mixture. In: ASCE Geo-Institute. Taylor & Francis 2024; London:524–527
25. Mighani HH, Tourchi S, Lavasan AA, Hosseini F, Szendefy J. Impact of plasticity and stress history on thermal volume changes in clays. *Scientific Reports.* 2025;15(1):19013.
26. Laloui L, Di Donna A, Witek M. Geothermal energy piles: thermal behaviour, geotechnical behaviour and applications. *Applied Energy.* 2014;117:292–303. doi: 10.1016/j.apenergy.2013.12.019
27. Zandarín MT. Thermo-Hydro-Mechanical Analysis of Joints: a Theoretical and Experimental Study. *PhD thesis.* 2010. ISBN: http://www.tdx.cat/TDX-1209110-120137.
28. Olivella S, Gens A, Carrera J, Alonso E. Numerical formulation for a simulator (CODE_BRIGHT) for the coupled analysis of saline media. *Engineering Computations.* 1996;13(7):87-112. doi: 10.1108/02644409610151575
29. Barton N, Bandis S, Bakhtar K. Strength, deformation and conductivity coupling of rock joints. *International Journal of Rock Mechanics and Mining Sciences & Geomechanics Abstracts.* 1985;22(3):121-140. doi: https://doi.org/10.1016/0148-9062(85)93227-9
30. Van Genuchten MT. A closed-form equation for predicting the hydraulic conductivity of unsaturated soils. *Soil science society of America journal.* 1980;44(5):892–898. Publisher: Soil Science Society of America.
31. Alonso E, Zandarín M, Olivella S. Joints in unsaturated rocks: Thermo-hydro-mechanical formulation and constitutive behaviour. *Journal of Rock Mechanics and Geotechnical Engineering.* 2013;5(3):200-213. doi: https://doi.org/10.1016/j.jrmge.2013.05.004
32. Di Donna A, Laloui L. Numerical analysis of the geotechnical behaviour of energy piles. *International Journal for Numerical and Analytical Methods in Geomechanics.* 2014;39:861–888. John Wiley & Sons, Ltd.